

Costa Rica Institute of Technology

Electronics Engineer School



Evaluation of Numerical Methods for Multi-GHz SAR Computation

Graduation Project Thesis for the Title of Electronic Engineer, Licentiate
Degree.

Jose Alberto Carballo Madrigal

Cartago, Costa Rica


June 2017

INSTITUTO TECNOLÓGICO DE COSTA RICA
ESCUELA DE INGENIERÍA ELECTRÓNICA
PROYECTO DE GRADUACIÓN
ACTA DE APROBACIÓN

Defensa de Proyecto de Graduación
Requisito para optar por el título de Ingeniero en Electrónica
Grado Académico de Licenciatura
Instituto Tecnológico de Costa Rica

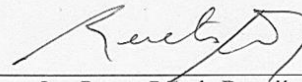
El Tribunal Evaluador aprueba la defensa del proyecto de graduación denominado Evaluation of Numerical Methods for Multi-GHz SAR Computation, realizado por el señor Jose Alberto Carballo Madrigal y, hace constar que cumple con las normas establecidas por la Escuela de Ingeniería Electrónica del Instituto Tecnológico de Costa Rica.

Miembros del Tribunal Evaluador



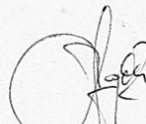
Ing. Anibal Coto Cortés

Profesor lector



Ing. Renato Rímolo Donadio

Profesor lector



Ing. Hayden Phillips Brenes

Profesor asesor

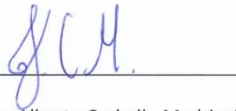
Cartago, 05 de junio, 2017

Declaration of Authenticity

I declare that this Graduation Project has been made, entirely by me, using and applying literature on the subject and introducing my own knowledge.

In cases where I have used the bibliographic material, I have proceeded to indicate the sources by referencing them.

Consequently, I take full responsibility for the graduation work done and the contents of the final report.



Jose Alberto Carballo Madrigal
Cartago, Costa Rica
19 Junio del 2017
ID: 2 0710 0057

Resumen

Palabras Claves: FIT, FEM, MoM, Altas frecuencias, SAR

En esta tesis se estudia la factibilidad de realizar simulaciones de onda completa para estimar el campo electromagnético absorbido en alta frecuencias, hasta 10 GHz, con solucionadores numéricos de propósito general y geometrías con tamaños en el orden de un cuerpo humano. Geometrías simples son analizadas, definiendo las propiedades del agua para su región interna. Tres diferentes métodos son evaluados: el método de integración finita (FIT), el método de elementos finitos (FEM) y el método de los momentos (MoM), con la intención de determinar la convergencia del resultado y los recursos computacionales necesarios en cada caso. Los resultados indican que a 10 GHz se torna difícil realizar dichos análisis con un recurso computacional moderado (hasta 70 GB RAM), pero algunas aproximaciones podrían ser explotadas debido a que la penetración del campo esta principalmente limitado a la región cercana a la superficie del objeto en ese rango de frecuencia.

Abstract

Keywords: FIT, FEM, MoM, High Frequencies, SAR

This work studies the feasibility of a full-wave simulation of field absorption at high frequencies, up to 10 GHz, with general purpose numerical methods and geometries with sizes in the order of a human body. Simple geometries are analyzed, assuming the material properties of water in the range of 1 to 10 GHz for its inner region. Three different methods are evaluated: the finite integration technique (FIT), finite element method (FEM), and method of moments (MoM), to determine the result convergence and required computational resources for each solution. The results show that already at 10 GHz is difficult to perform the analysis with moderate computational power (up to 70 GB RAM), but some approximations might be exploited since field penetration is mostly limited to the surface region in those ranges.

Outline

| | |
|---|----|
| 1. Introduction | 1 |
| 2. Theoretical Background | 3 |
| 2.1 Electromagnetics Fundamentals | 3 |
| 2.2 Specific Absorption Rate | 4 |
| 2.3 Electrical Properties of the Materials | 5 |
| 2.4 Computational Electromagnetics | 7 |
| 2.4.1 Finite Integration Technique (FIT) | 8 |
| 2.4.2 Method of Moments (MoM) | 9 |
| 2.4.3 Finite Element Method (FEM) | 11 |
| 3 Geometrical Models Description and Implementation | 12 |
| 3.1 Dimensions of the models | 12 |
| 3.2 General Setup for Geometrical Models | 14 |
| 3.3 The excitation | 14 |
| 3.4 The material: Water | 15 |
| 3.5 Observation points definition and quantities in the analysis | 15 |
| 3.6 Lambda Refinement, Mesh, and other Considerations | 17 |
| 3.7 Models Considerations with Regard to Specific Frameworks | 19 |
| 3.7.1 CONCEPT-II Model Specifications | 19 |
| 3.7.2 CST Model Specifications | 22 |
| 3.7.3 HFSS model Specifications | 25 |
| 4. Simulation Results with Regard to Electric Field Penetration | 29 |
| 4.1 Sphere | 29 |
| 4.1.1 Sphere Model Results at 1 GHz | 29 |
| 4.2 Small Ellipsoid | 32 |
| 4.2.1 Small Ellipsoid Model Results at 1 GHz | 32 |
| 4.2.2 Small Ellipsoid Model Results at 10 GHz | 33 |
| 4.3.1 Large Ellipsoid Model Results at 1 GHz | 34 |
| 4.3.2 Large Ellipsoid Model Results at 3 GHz | 35 |
| 5. Simulation Results | 37 |
| 5.1 Simulation Results with Regard to Field Behavior | 37 |

| | |
|---|-------------|
| 5.2 Comparison of Computational Effort | 42 |
| 5.3 Comparison of Electric Field Penetration and Variation of the Material Conductivity..... | 47 |
| 6. Conclusions and Recommendations | 51 |
| References | 53 |
| Appendix A: Additional Results | i |
| A.1 Sphere Model Results at 2 GHz..... | i |
| A.2 Sphere Model Results at 5 GHz..... | ii |
| A.3 Sphere Model Results at 7 GHz..... | iii |
| A.4 Small Ellipsoid Model Results at 2 GHz..... | iv |
| A.5 Small Ellipsoid Model Results at 5 GHz..... | v |
| A.6 Small ellipsoid model results at 7 GHz | vi |
| A.7 Sphere at 1 GHz Electric Field Distribution | vii |
| A.8 Sphere at 5 GHz Electric Field Distribution | vii |
| A.9 Small Ellipsoid at 1 GHz Electric Field Distribution..... | viii |
| A.10 Small Ellipsoid at 2 GHz Electric Field Distribution | viii |
| A.11 Small Ellipsoid at 5 GHz Electric Field Distribution | viii |
| A.12 Large Ellipsoid at 1 GHz Electric Field Distribution | ix |

List of Figures

| | |
|--|----|
| Figure 2. 1 Boundary conditions for general media interface. Taken from [2] | 7 |
| Figure 2. 2 An example of the grid cell. This figure is an example of a cell complex G define by $V_{i,j,k} - 1$ with the allocation of the electric grid voltages on the edges of A (different color surface) and the magnetic facet flux through A. Taken from [13] | 8 |
| | |
| Figure 3. 1 General set up for the Large Ellipsoid. In this Figure is shown in yellow the orientation of the plane wave(excitation) and in blue the orientation of the coordinate axis in space. | 14 |
| Figure 3. 2 Definition of the trajectory AB and CD for the sphere model..... | 16 |
| Figure 3. 3 Definition of the trajectory AB and CD for the small ellipsoid model..... | 16 |
| Figure 3. 4 Definition of the trajectory AB and CD for the large ellipsoid model | 17 |
| Figure 3. 5 Mesh quality. Is shown how the surface of the model changing due the variation of how many elements are required to describe the surface itself, is notable that in case of the increase of elements more smooth and accurate the surface will be generated..... | 19 |
| Figure 3. 6 Sphere model at 1 GHz of the generated model and mesh by CONCEPT-II CAD tool | 20 |
| Figure 3. 7 The sphere model quarter in CONCEPT-II. | 20 |
| Figure 3. 8 Generation of the surface and mesh configuration. | 21 |
| Figure 3. 9 Definition of the bounding box in CST..... | 23 |
| Figure 3. 10 Mesh plot generated by CST in the sphere model at 10 GHz | 23 |
| Figure 3. 11 CST Time domain solver set up | 24 |
| Figure 3. 12 Mesh generated by HFSS in the bounding box at sphere model at 1 GHz | 25 |
| Figure 3. 13 Boundary condition in HFSS at the bounding box at sphere model at 1 GHz..... | 25 |
| Figure 3. 14 Mesh generated by HFSS in the sphere model at 1 GHz..... | 26 |
| Figure 3. 15 Definition of the solver set up for the sphere model at 1 GHz | 26 |
| Figure 3. 16 Convergence and energy condition for the sphere at 1 GHz..... | 27 |
| | |
| Figure 4. 1 S model: E^2 of the E_z -Field over the x-axis at 1 GHz | 29 |
| Figure 4. 2 S model: E^2 of the E_z -Field over the z.axis..... | 30 |
| Figure 4. 3 S model: E^2 of the E-Field over the x-axis at 10 GHz..... | 31 |
| Figure 4. 4 S model: E^2 of the E-Field over the z-axis at 10 GHz..... | 31 |
| Figure 4. 5 SE model: E^2 of the E-Field over the x-axis at 1 GHz..... | 32 |
| Figure 4. 6 SE model: E^2 of the E-Field over the z-axis at 1 GHz..... | 32 |
| Figure 4. 7 SE model: E^2 of the E-Field over the x-axis at 10 GHz..... | 33 |
| Figure 4. 8 SE model: E^2 of the E-Field over the z-axis at 10 GHz..... | 33 |
| Figure 4. 9 LE model: E^2 of the E-Field over the z-axis at 1 GHz | 34 |
| Figure 4. 10 LE model: E^2 of the E-Field over the z-axis at 1 GHz | 35 |
| Figure 4. 11 LE model: E^2 of the E-Field over the x-axis at 3 GHz..... | 35 |
| Figure 4. 12 LE model: E^2 of the E-Field over the z-axis at 3 GHz..... | 36 |
| | |
| Figure 5. 1 XZ plane, E-field behavior for the sphere model at 1 GHz..... | 37 |
| Figure 5. 2 XZ plane field behavior sphere model at 10 GHz..... | 38 |

| | |
|---|----|
| Figure 5. 3 XZ plane E-field behavior sphere model at 10 GHz zoom and visualization of small values (red arrows)..... | 38 |
| Figure 5. 4 XZ plane E-field behavior small ellipsoid model at 10 GHz | 39 |
| Figure 5. 5 XZ plane E-field behavior large ellipsoid model at 1 GHz..... | 40 |
| Figure 5. 6 Configuration to plot the behavior at a specific area of the large ellipsoid at 1 GHz | 40 |
| Figure 5. 7 Plot xz plane for the setup shown in Figure 5.6 as a close up to the plot..... | 41 |
| Figure 5. 8 Plot xz plane for the setup shown in Figure 5.6 as a detail to observe boundary conditions..... | 41 |
| Figure 5. 9 Current distribution for the LE at 2 GHz..... | 42 |
| Figure 5. 10 Comparison of the memory consumption for the sphere model | 44 |
| Figure 5. 11 Comparison of computing time for the sphere model | 44 |
| Figure 5. 12 Comparison of the memory consumption for the small ellipsoid model | 45 |
| Figure 5. 13 Comparison of computing time for the small ellipsoid model..... | 45 |
| Figure 5. 14 Comparison of the memory consumption for the large ellipsoid model..... | 46 |
| Figure 5. 15 Comparison of computing time for the large ellipsoid model | 46 |
| Figure 5. 16 S model: Magnitude of the Ez-Field over the x-axis at different frequencies..... | 47 |
| Figure 5. 17 SE model: Magnitude of the Ez-Field over the x-axis at different frequencies..... | 48 |
| Figure 5. 18 LE model: Magnitude of the Ez-Field over the x-axis at different frequencies..... | 48 |
| Figure 5. 19 LE model: Magnitude of the Ez-Field over the z-axis at different frequencies..... | 49 |
| Figure 5. 20 LE model: E^2 of the E-Field over the x-axis at 3 GHz with different conductivities | 50 |
| Figure 5. 21 LE model: E^2 of the E-Field over the z-axis at 3 GHz with different conductivities..... | 50 |

List of Tables

| | |
|--|----|
| Table 2. 1 The variations of exposure limits to RF radiation in several countries..... | 4 |
| Table 2. 2 A comparison of the FCC and ICNIRP local SAR limits in the head and trunk for the general public | 5 |
| Table 2. 3 Comparison between FIT, FEM, and MoM as numerical techniques..... | 7 |
| Table 3. 1 Summary of models dimensions | 14 |
| Table 3. 2 Summary of the trajectories for the three geometries (Sphere: S, Small Ellipsoid: SE, Large Ellipsoid: LE)..... | 17 |
| Table 3. 3 Summary of CONCEPT-II simulations | 22 |
| Table 3. 4 Summary of CST simulations | 24 |
| Table 3. 5 Summary of HFSS simulations | 27 |
| Table 5. 1 Comparison of the computational resources necessary for all used tools | 43 |

List of abbreviations

| | |
|-------|--|
| AB | Trajectory over the x-axis from A to B |
| AB_LE | Trajectory over the x-axis from A to B for the large ellipsoid model |
| AB_S | Trajectory over the x-axis from A to B for the sphere model |
| AB_SE | Trajectory over the x-axis from A to B for the small ellipsoid model |
| CD | Trajectory over the z-axis from C to D |
| CD_LE | Trajectory over the z-axis from C to D for the large ellipsoid model |
| CD_S | Trajectory over the z-axis from C to D for the sphere model |
| CD_SE | Trajectory over the z-axis from C to D for the small ellipsoid model |
| FEM | Finite element method |
| FIT | Finite integration technique |
| LE | Largó Ellipsoid model |
| MOM | Method of moments |
| O | Center or Origin of the model (0,0,0) |
| S | Sphere model |
| SAR | Specific Absorption Rate |
| SE | Small Ellipsoid model |

Acknowledgements

Esta tesis represento un reto académico, pero también un reto personal que sin la ayuda de la calidez de mi formación como ser humano este conocimiento jamás se hubiera logrado de una manera tan gratificante.

Agradezco a mis padres Flor y Ronald, ambos presentes constantemente en mi vida. Mi madre por brindarme una calidez humana increíble capaz de entender lo inentendible y brindarme las herramientas para ser empático. A mi padre por siempre apoyarme en todas las situaciones de mi vida sin poner excusas y por las lecciones de vida aprendidas.

A mis hermanas: Joha y Naty por brindarme experiencias de vida y reglas de convivencia de las cuales hoy en día me ayudan a realizar todo lo que puedo y por protegerme cuando la ocasión se presentaba.

A mi hermano David, le agradezco por forjar mi carácter y demostrarme que tengo la capacidad para afrontar los miedos con valentía, carisma y sabiduría.

Al Profesor Renato Rímolo Donadío por brindarme la oportunidad de desarrollar este tema de tesis, asesorarme y guiarme durante este trayecto, que sin él hubiese sido imposible lograrlo. Muchas gracias por su tiempo y calidad personal y profesional que no para de sorprenderme y admirarme.

Kim gracias por brindarme las mejores experiencias de mi vida durante este trayecto por su apoyo, calidez, amor, paciencia y presencia constante. Por enseñarme tanto en tan poco tiempo. De no ser por su sacrificio y constante entrega esta experiencia no hubiese resultado.

A todos los profesores y compañeros que estuvieron presentes durante mi formación académica en el ITCR, que sin ellos el camino a seguir y el conocimiento generado sería una sombra de lo que poseo hoy en día.

I would also like to thank all TET staff for their charisma, professionalism and incredible personality. Especially to Prof. Schuster and Heinz both for giving me an incredible life experience with academic teachings. I thank you deeply for showing me that academic world and lifestyle.

1. Introduction

Exposition of humans to non-ionizing radiation at high frequencies has become ubiquitous due to the higher number of systems operating in that frequency range such as cell phones, wireless networks, and communication systems [1]. The modeling of the impact of this type of radiations is an important issue due to potential long-term health effects and for the definition of regulatory safety limits [1] [2][3].

The calculation and analysis of the specific absorption rate (SAR) have been used as a metric to assess the amount of energy absorbed by human beings due to the exposure of electromagnetic radiation to establish safety limits [1] [2]. Although the health effects are known for ionizing radiation and high power fields [4] [1], SAR is also used to define safety radiation limits for non-ionizing [5] [6], even though long-term exposure to EM radiation is not so well understood.

From the simulation point of view, SAR evaluation at frequencies in the deep Gigahertz range has not been explored in detailed since the wavelengths of interest are much smaller than the typical dimensions of a human body. This wavelength comparison leads to the requirement of very fine discretization of the geometrical models and the consequent high demand for computational resources and long execution times.

To evaluate the capabilities of full wave solvers to estimate SAR in the GHz range, this work presents an analysis comparing different numerical codes. The first implementations developed are in Computer Simulation Technology (CST) [7], and High-Frequency Electromagnetic Field Simulation (HFSS) [8], which are both commercial tools and are based on FIT and FEM numerical techniques, correspondingly; a third implementation was carried out in CONCEPT-II [9], an in-house academic tool at the Hamburg University of Technology (TUHH) based on MoM. Computational requirements regarding numerical efficiency and convergence of the solutions obtained are evaluated as well. For this purpose, simulation models representative of the human body when exposed to radiation were constructed, which can be used to analyze the phenomenon of diffraction and absorption with numerical techniques. To fulfill this, it was necessary to generate geometrical models representative of the human body, in dimensions and shape, suitable for electromagnetic simulation in the GHz range.

The work is organized in six chapters. Chapter 2 addresses Bioelectromagnetics fundamentals that consist of a brief review of electromagnetics, the definition of SAR, and basic description of the three numerical techniques. Chapter 3 discusses the methodology to compare the different codes and the final simulation results. Also, Chapter 3 include a description of the geometrical models and the implementation of each code. Chapter 4 compares the final numerical results with the evaluated in the range of 1 up to 10 GHz, with the three geometrical models selected: a sphere, ellipsoid, and a large ellipsoid. Chapter 5 discusses the validation of the results,

comparing the ones obtained with the three codes. Finally, Chapter 6 summarizes the conclusions and recommendations for further research.

2. Theoretical Background

2.1 Electromagnetics Fundamentals

Computational electromagnetics, known as CEM, deals with the numerical approximated solution of Maxwell's equations to calculate electric and magnetic fields in the presence of arbitrary geometries and material definitions. Many different alternatives and methods to electromagnetic simulation are available, each of them showing advantages and disadvantages to solve certain types of problems. Depending on which technique is used to the calculated the approximation of these quantities, Maxwell equations are required in their integral or differential form. These are Maxwell's equations in both forms:

$$\oint \vec{D} \cdot d\vec{S} = \int_V \rho_V dV \quad (1) \quad \nabla \cdot \vec{D}(\vec{r}, t) = \rho_V(\vec{r}, t) \quad (5)$$

$$\oint \vec{E} \cdot d\vec{L} = -\frac{d}{dt} \int \vec{B} \cdot d\vec{S} \quad (2) \quad \nabla \times \vec{E}(\vec{r}, t) = \frac{\partial B(\vec{r}, t)}{\partial t} \quad (6)$$

$$\oint \vec{B} \cdot d\vec{S} = 0 \quad (3) \quad \nabla \cdot \vec{B}(\vec{r}, t) = 0 \quad (7)$$

$$\oint \vec{H} \cdot d\vec{L} = I + \int \frac{\partial \vec{D}}{\partial t} \cdot d\vec{S} \quad (4) \quad \nabla \times \vec{H}(\vec{r}, t) = \vec{J}(\vec{r}, t) + \frac{\partial D(\vec{r}, t)}{\partial t} \quad (8)$$

where:

\vec{E} : Electric field intensities V/m

\vec{H} : Magnetic field intensities A/m

\vec{D} : Electric flux densities C/m²

\vec{B} : Magnetic flux densities Wb/m²

\vec{J} : Electric charge density A/m²

ρ_V : Volume charge density C/m³

There are many different techniques to compute electromagnetic fields in CEM. The numerical techniques or codes used in this report are FEM [7], FIT [8] and MOM [9]. These three methods will be briefly described later.

2.2 Specific Absorption Rate

As a metric to evaluate the field absorption, the specific absorption rate, SAR, is a quantity that is often used in relation to biological tissue. There are different standards and relationships to quantify SAR depending on the mass of the material and the distance from the body to the source [1][2]. The relation related used in this investigation is the point SAR:

$$\frac{1}{V} \iiint \frac{\sigma(r)|E(r)|^2}{\rho(r)} dr \quad (9)$$

Where $\sigma(r)$ is the conductivity of the material, $\rho(r)$ is the mass density of the material, and $|E(r)|^2$ is the magnitude of the electric field, as a function of the position r . Since the models used in this work have constant conductivity and density, the results are evaluated in terms of the square magnitude of the electric field only. Information on electromagnetic properties of the materials and densities can be found in [10] [11] and [12].

In the literature related to this topic exist different standards and SAR measurements. The following image summarizes some standard and guidelines defined in different countries:

Table 2. 1 The variations of exposure limits to RF radiation in several countries.

| Country/Guidelines | PD Restrictions for the General Public in W/m^2 | PD Restrictions for the General Public in mW/m^2 | Frequency Range (GHz) | Basic |
|--------------------|---|--|-----------------------|---------------|
| INCRP(1998) | 10 | 1 | 2-300 | Science Based |
| FCC(1996) | 10 | 1 | 105-100 | Science Based |
| China(1987) | 0.1 | 0.01 | 0.3-300 | Science Based |
| Russia(2003) | 0.1 | 0.01 | 0.3-300 | Science Based |
| Switzerland | 0.1 | 0.01 | 1.8-300 | Precautionary |
| Italy | 0.1 | 0.01 | 0.0001-300 | Precautionary |

Table information is taken from [2]

The most common standards are the ones from the Federal Communications Commission (FCC) which is used in the United States and the International Commission on Non-Ionizing Radiation Protection (ICNIRP) which is defined in Europe.

Related to SAR measurement and general SAR equation (1), there are the following different SAR-related quantities known as Whole-Body Average SAR, Local SAR and Point SAR. For Whole-Body Average SAR and Local SAR one of the main

features is that the volume is considered for the power computation. For example, according to [1], the Whole-Body Average SAR considers the overall volume of the body and for Local SAR considers a proportion of the body for example limbs, trunk, and head. Local SAR also takes into consideration the amount of volume in which the power is dissipated. Related to the Guidelines FCC and ICNIRP, Table 2 resume this consideration to Local SAR.

Table 2. 2 A comparison of the FCC and ICNIRP local SAR limits in the head and trunk for the general public

| Exposure Standard | SAR Limits for Near-Field Exposure | RF | Frequency Range (MHz) | Averaging Volume |
|-------------------|------------------------------------|----|-----------------------|--|
| ICNIRP | 2 | | 10-10000 | “any 10g of contiguous tissue (10 g SAR)” |
| FCC | 1.6 | | 0.1-6000 | “any 1g of tissue defined as a tissue volume in the shape of a cube (1 g SAR)” |

Table information is taken from [1]

In this thesis, the SAR measurement used is the Point SAR relation which is represented as it follows:

$$\frac{\sigma(r)|E(r)|^2}{\rho(r)} = SAR_{POINT} \quad (10)$$

The main consideration to use this kind of measurement is the nature of the experimentation and to the fulfillment of the objectives. The point SAR can compare specific points in space with each code and validated the convergence of the solutions proposed for each model.

This equation is a point relation; the model developed in this report have constant conductivity and density all over the model in order to reduce the complexity of the model and the computational requirements.

2.3 Electrical Properties of the Materials

The behavior of a wave in lossy materials, compared to a wave traveling in free space, is modified because of the electrical properties of the media. In this specific case, the interface between water [10] and the air is considered.

The equation for the representation of a harmonic plane wave for the electric field in lossy media, propagating in the z-direction can be written as [13]:

$$E_x = E_{x0} e^{-\alpha z} \cos(\omega t - \beta z) \quad (11)$$

where t represents time, ω is the angular velocity and E_{x0} is the complex vector amplitude of the field. The propagation constant is defined as $\gamma = jk = \alpha + j\beta$ with:

$$\alpha = \omega \sqrt{\frac{\mu \epsilon'}{2}} \left[\sqrt{1 + \left(\frac{\epsilon''}{\epsilon'}\right)^2} - 1 \right] = \text{Attenuation constant} \quad (12)$$

$$\beta = \omega \sqrt{\frac{\mu \epsilon'}{2}} \left[\sqrt{1 + \left(\frac{\epsilon''}{\epsilon'}\right)^2} + 1 \right] = \text{propagation constant} \quad (13)$$

where ϵ' and ϵ'' denotes real and imaginary part of the permittivity, respectively.

It is also relevant to express that the skin depth phenomenon is fundamental to the understanding of the report. The basic relation between the field behavior in relation to the skin effect is defined as the characteristic skin depth for non-magnetic materials:

$$\text{Skindepth} = \frac{1}{\alpha} = \sqrt{\frac{2}{\omega \mu_0 \sigma}} \quad (14)$$

The Skin effect phenomena could be understood as the penetration of the E-field inside the body. The Skin effect is a quantity with a frequency dependency which distributes a larger portion of the power to be concentrated at the surface of the model with the increase of frequency.

Also, it is necessary to describe the boundary conditions for lossy media because this represents a condition required in each solution for validation. The boundary relevant condition can be written as:

$$D_{n1} = D_{n2} \quad (15)$$

$$E_{T1} = E_{T2} \quad (16)$$

with D as the dielectric flux density and sub-indexes "n" and "T" indicating the normal and tangential components, respectively. This is illustrated in Figure 2.1:

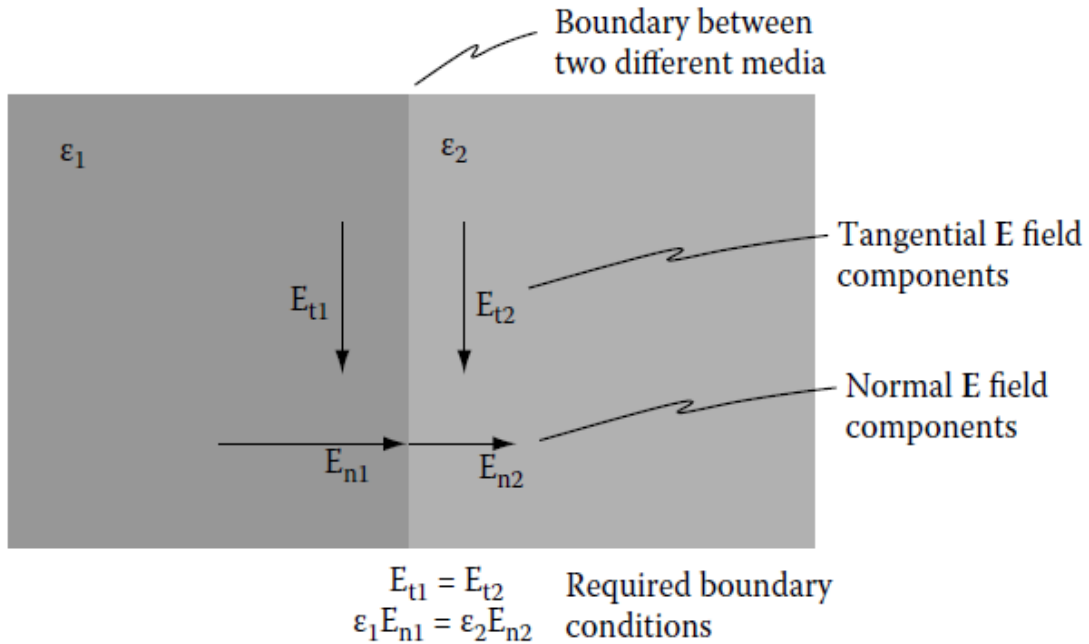


Figure 2. 1 Boundary conditions for general media interface. Taken from [2]

2.4 Computational Electromagnetics

As mentioned in section 2.2 the CEM use different discretization schemes and formulations of Maxwell equations to obtain a numerical approximation of electromagnetic phenomena. This section presents a brief review of each numerical technique used in this work to understand their background and the construction of the solution itself as a numerical technique. Table 2.3 shows the main features of the three methods discussed.

Table 2. 3 Comparison between FIT, FEM, and MoM as numerical techniques

| Formulation | Equation Type | Domain | Type of technique |
|-------------|---------------|-----------|-------------------|
| FIT | Integral | Time | Volume |
| FEM | Differential | Frequency | Volume |
| MoM | Integral | Frequency | Surface |

2.4.1 Finite Integration Technique (FIT)

The Finite Integration Technique is the base of CST Microwave Studio solver. Weiland et al. developed it in 1977 [14]. FIT is a discrete formulation of Maxwell's equations capable of solving electromagnetic problems by computers [15]. The FIT technique is a volume technique; this means that the first step is to restrict the volume and the second step is the decomposition of the restricted space in a finite number of "cells." These "cells" are formally called grid cell complex G , and the restricted space is referred as $\Omega \in R^3$ [14]. G can be described as:

$$G := \{V_{i,j,k} \in R^3 \mid V_{i,j,k} := [x_i, x_{i+1}]x[y_i, y_{i+1}]x[z_i, z_{i+1}]\} \quad (17)$$

$$i = 1, \dots, I - 1, j = 1, \dots, J - 1, k = 1, \dots, K - 1$$

It can be represented in the following graphical structure:

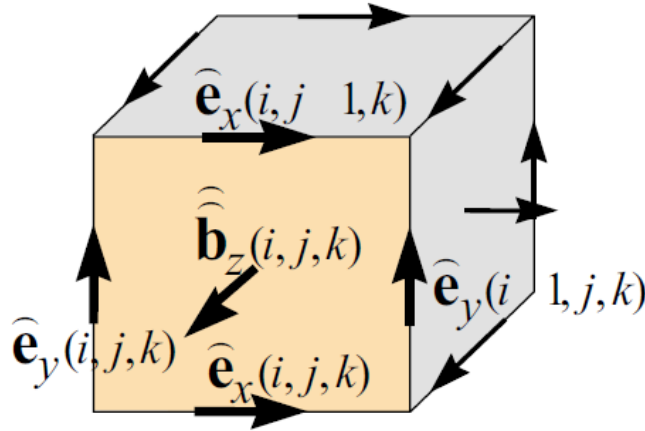


Figure 2. 2 An example of the grid cell. This figure is an example of a cell complex G define by $V_{i,j,k-1}$ with the allocation of the electric grid voltages on the edges of A (different color surface) and the magnetic facet flux through A. Taken from [13]

The construction of the matrix-vector can be related to an example as in Figure 2.2, which is related to the integral form of Faraday's Law, equation (4). The construction of this matrix-vector for each complex cell G requires the definition of the following: discrete curl operator (C), discrete divergence operator (S) and the definition of a dual complex mesh called \tilde{G} for the definition of the matrix discrete form of Ampere's Law and Gauss's Law. With the fulfillment of the mentioned the complete set of resulting equations are called Maxwell's Grid Equations (MGE) which are the discretization of the Maxwell's equations. The following are described by the following relations:

Maxwell Grid Equations (MGE)

$$e = -\frac{d}{dt}b \quad (18)$$

$$\check{C}h = \frac{d}{dt}b + j \quad (19)$$

$$\check{S}d = q \quad (20)$$

$$Sb = 0 \quad (21)$$

Equation 18 to 21 can be collected in a matrix form. For example, equation 18 becomes:

$$\begin{pmatrix} \dots & \dots & \dots \\ 1 & \dots & -1 \\ \dots & \dots & \dots \end{pmatrix} \begin{pmatrix} e_{n1} \\ \vdots \\ e_{n4} \end{pmatrix} = \frac{d}{dt} \begin{pmatrix} \vdots \\ b_n \\ \vdots \end{pmatrix} \quad (22)$$

The discretization of Maxwell equation to MGE has been done, and all the information is from integral state variables on points (potentials), edges(voltages), surfaces(fluxes) and volume (charges) [14]. But the definition of the material equations averaged over the cells areas and edges is needed to relate two different cells. These equations are:

$$d = M_\varepsilon e + p \quad (23)$$

$$b = M_\mu h - m \quad (24)$$

$$j = M_\sigma e \quad (25)$$

2.4.2 Method of Moments (MoM)

The Method of Moments (MoM) has been used in electromagnetics since the work of R.F. Harrington in [16] and [17]. It is a general procedure for the transformation of an operator equation into a linear system capable of being solved by a computer. The general form of the equations is:

$$L u = g \quad (26)$$

L: Linear operator

u: unknown function

g: known excitation function

As an example, the ideal conducting body of a wire is explained. In this specific case, the linear operator is the electric field integral equation (EFIE). The EFIE mixed integral formulation is:

$$\vec{n} \times \left\{ \frac{1}{4\pi} \iint_S \left[j\omega\mu\vec{J}_s \frac{e^{-jkR}}{R} + \frac{\text{div}\vec{J}_s}{\omega\epsilon} \text{grad} \frac{e^{-jkR}}{R} \right] ds \right\} = \text{EFIE} \quad (27)$$

Once the linear operator that relates the unknown current distribution and the impressed field is defined, the main goal of the method is to solve the operator equation.

The boundary condition for a metallic body is defined as:

$$\vec{E}_{tan} = \vec{E}_{tan}^{inc} + E_{tan}^{sca} = 0 \quad (28)$$

$$\vec{n} \times \vec{E}^{inc} = \vec{n} \times \left\{ \frac{1}{4\pi} \iint_S \left[j\omega\mu\vec{J}_s \frac{e^{-jkR}}{R} + \frac{J\text{div}\vec{J}_s}{\omega\epsilon} \text{grad} \frac{e^{-jkR}}{R} \right] ds \right\} \quad (29)$$

The solution of the problem is accomplished by the definition of the operator equation into a matrix equation as it follows:

$$L(l(z')) = \vec{E}^{inc} \quad (30)$$

According to the boundary conditions the $\vec{E}^{inc} = 0$, each point on the surface of the structure is related to the scattered tangential electric field strengths caused by current distribution J_s , which has to cancel to the tangential incident field.

To fulfill this boundary condition, the creation of basis functions (equation (31)) are necessary to model surface electric current densities. The basis functions are responsible for forcing the solution to have a residual error reduced to zero. This procedure is called testing or weighting process [18] (equation (32)).

$$l(z') = \sum_{n=1}^N l_n f_n(z') \quad (31)$$

$$R = \vec{E}^{inc} - L(l(z')) = \text{Residual error} \quad (32)$$

Using point matching these integral equations are transformed to:

$$(Z) \cdot (I) = (U) \quad (33)$$

Where (Z) as the impedance matrix, (I) vector with the unknown complex current amplitudes and (U) as the voltage vector known. This can be compare to the form of equation (26) [19].

In the case of the treatment of dielectric bodies, the boundaries conditions to fulfill are:

$$E_{T1} = E_{T2} \quad (34)$$

$$H_{T1} = H_{T2} \quad (35)$$

This change for the boundary conditions will lead to twice the number of unknowns, taking as a reference to the approach developed by a conductive body.

2.4.3 Finite Element Method (FEM)

The Finite Element Method is also known as Finite Element Analysis (FEA). This is a volume technique. Thus it is necessary to restrict the integration space and the discretization of the space with a finite number of elements. The treatment of the equations can be formulated by the variational method or weighted residual.

The variational method (Ritz Method) [20] is a condition that seeks the fulfillment of an energy criteria. In this case, 3D time-harmonic EM problem is used as shown:

$$\int_v \left\{ \mu \frac{|H|^2}{2} + \varepsilon \frac{|E|^2}{2} - \frac{J \cdot E}{2J\omega} \right\} dV \quad (36)$$

3 Geometrical Models Description and Implementation

Simple geometrical models were defined to be evaluated with the methods, focusing on the required effort to obtain convergent results in all simulations. The procedure of comparison was to calculate the electric field inside the body along probe lines. Also, an analytical solution for the case of a sphere was used [21].

The comparison between the computational resource needs in each tool to obtain comparable results in every solution related to the analytical solution by the generation of a proper mesh and the elimination of unwanted non-physical behavior related to a deficient simulation setting.

Another aspect of assessing the quality of the results is the validation of expected physics. This can be carried out, for example, by 2D views of electric field distributions. Plots of the E-field behavior at different phases can reflect velocity of propagation, boundary condition enforcement, wavelength related maxima and minima, resonances, field penetration, and distribution, among others.

For the sake of being capable of comparing the results of all codes used, each simulation have to be done in a single frequency because in the case of using a sweep in frequency the mesh has to be discretized to the maximum frequency of the analysis. This means that in the case of doing a sweep from 1 to 3 GHz, the mesh has to be fine enough to be capable of generated good results at 3 GHz, but for 1 GHz the mesh will be too fine. Thus, the memory consumption could not be comparable to each tool and point. Another reason is that the amount of information retrieved from commercial tools is limited. In case a sweep is done, the metric returns the final memory consumption, not always the individual for each point in frequency.

For the current work, it is necessary the establishment of different models for experimentation and representation of the human body in a simple manner, which compare the tradeoff between the scale of the model, accuracy and computation efforts.

It is relevant to understand how each method analyzes different geometries and the possible problems in the final solution about numerical efficiently and physical validation. In this section, the geometrical setup is detailed as well as the excitation configuration. The electrical properties of the material, mesh, number of unknowns, and specific annotations for each framework are considered.

Three geometrical models used in this project: a sphere, a “small” ellipsoid and a “large” ellipsoid. Dimensions and proper parameterization are discussed in the next sections.

3.1 Dimensions of the models

The selection of the geometrical model is based on a strong simplification of human anatomy. In the first case, a sphere geometry allusive to the average adult human head size is considered. For the second case and third cases, ellipsoidal geometries

are considered, with a size that resembles the size of a young child and the whole body of an average adult (Furse, 2009).

The sphere is the first model considered, being the simplest model, the discussion here can be related to the following ellipsoidal models. The selection of this geometry as a starting point is due to the dimension of the model itself, being the smallest of the three models, and because there is an analytical solution available [21]. The equation that describes a sphere is the typical cartesian relationship:

$$x^2 + y^2 + z^2 = r^2 \quad (37)$$

The complexity of the model increases by the selection of next geometry; the sphere is the simplest geometry in this work that can be related to a human body, which resembles the whole structure as in [5]. The characteristic parameterization in cartesian coordinates is:

$$x = a \cos(u) \cos(v) \quad (38)$$

$$y = b \cos(u) \sin(v) \quad (39)$$

$$z = c \sin(u) \quad (40)$$

where:

$$\frac{-\pi}{2} \leq u \leq \frac{\pi}{2} \wedge -\pi \leq v \leq \pi$$

Also, the values of the constants are related to the following orientations: a has an orientation on the x-axis, b has an orientation on the y-axis and c has an orientation on the z-axis.

For simplicity, the values of a and b are equal. The only difference between the large and the small ellipsoid is the dimension of a , b and c related to equations (38), (39) and (40). For the small case a and b are 5 cm and c 30 cm. For the large case a and b , is 15 cm and c 90 cm.

Table 3.1 is a summary of the dimensions of each model, with each progression the geometry gets closer to a human body related geometry. The ellipsoid, have the same cross section over the x-axis and y-axis, but the z-axis is then increased to resembles the height of an average human in the large ellipsoid. Final dimensions are summarized in Table 3.1.

Table 3. 1 Summary of models dimensions

| Model | Radius (cm) | Height (m) |
|-----------------|-------------|------------|
| Sphere | 10 | --- |
| Small Ellipsoid | 10 | 0,6 |
| Large Ellipsoid | 15 | 1,8 |

3.2 General Setup for Geometrical Models

For all different models in every tool, the excitation and the electrical parameters of the material were the same (water, detailed next). Also, the location in space and the distance between the body and the excitation use the same definition to get more consistent results for comparison purposes.

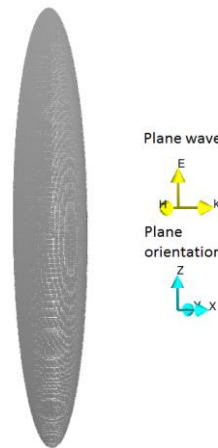


Figure 3. 1 General set up for the Large Ellipsoid. In this Figure is shown in yellow the orientation of the plane wave(excitation) and in blue the orientation of the coordinate axis in space.

3.3 The excitation

For the excitation of all models is a plane wave with the following features:

- Linear polarization.
- Propagates in the x+.
- Polarized (E-vector) in z+.
- Amplitude 1[V/m]

The polarization of the plane wave, E polarization, is chosen because of the effect on the overall structure. As mentioned in [2], this is the polarization that gave the strongest effects related to the E-field inside the body.

3.4 The material: Water

The material by itself is a vast topic about different parametric models, regarding the content of water in tissue, polarization, and other related quantities, as it is mentioned in [1]. Using an extreme simplification, the human body is described as a mass of fresh water. The electrical properties of water can be found in [10], as a default set up in the following electrical properties used are:

- Relative permittivity: 78.
- Relative permeability: 1.
- Density: 1000 [Kg/m].
- Conductivity: 1.59 [S/m].

3.5 Observation points definition and quantities in the analysis.

For the numerical techniques, there is a limit where the resolution of the code estimates 0, values with a small numeric representation, which is denominated the numerical noise floor. Also, it is relevant to plot the magnitude square of the electric field which resembles power within the body or surface and is directly related to the point SAR, as mention in section 2.2 and equation (10). The reason to plot power instead of direct SAR is for validation purposes because is possible to see the fulfillment of the boundaries conditions and since the material is homogeneous, SAR is proportional to the square of the field intensity.

For this purpose, a probe line along the geometries was created. The length of each probe line is different, and also it is necessary to have more or less length and more or fewer observation points accordingly (the reason for this will be explained in the following sections). In the following, this probe line will be called AB and CD for the x-axis and z-axis, respectively.

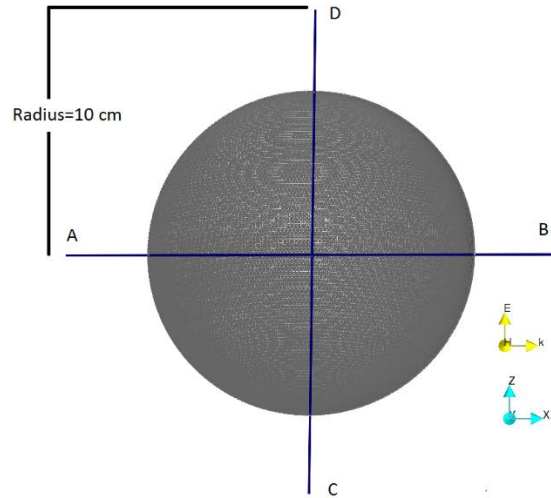


Figure 3. 2 Definition of the trajectory AB and CD for the sphere model

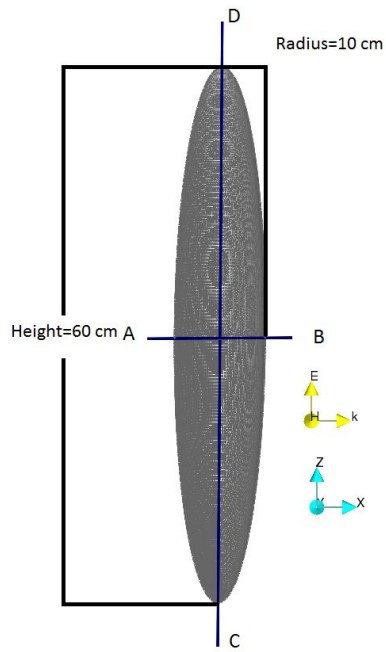


Figure 3. 3 Definition of the trajectory AB and CD for the small ellipsoid model

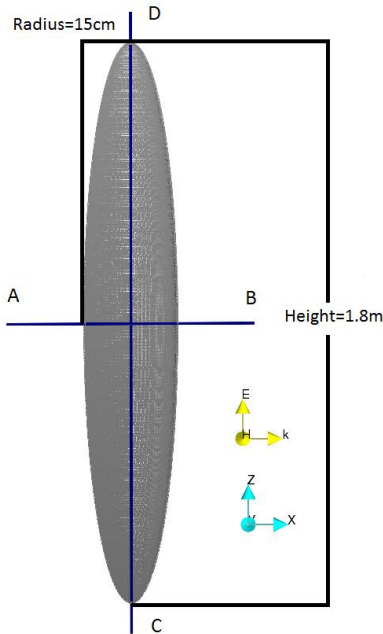


Figure 3. 4 Definition of the trajectory AB and CD for the large ellipsoid model

The quantities and values that delimit and describe each path along the axis in the different models are summarized in Table 3.2

Table 3. 2 Summary of the trajectories for the three geometries (Sphere: S, Small Ellipsoid: SE, Large Ellipsoid: LE)

| Name | Length (cm) | From | To | Axis |
|-------|-------------|------|-----|------|
| AB-S | 30 | -15 | 15 | X |
| AB-SE | 16 | -8 | 8 | X |
| AB-LE | 100 | -50 | 50 | X |
| CD-S | 30 | -15 | 15 | Z |
| CD-SE | 70 | -35 | 35 | Z |
| CD-LE | 200 | -100 | 100 | Z |

3.6 Lambda Refinement, Mesh, and other Considerations.

This section deals with the troubleshoot analysis for the creation of the proper mesh to get numerical and physical related results. The settings for the creation of a proper mesh to get accurate numerical and physical related results are one of the main concerns for a proper simulation execution, as the model regions are much larger than the internal wavelength. Some of the points to take in consideration, among

others, are the lambda specific mesh (cell), the roughness of the surface and unphysical behaviors due to insufficient discretización.

For every model, it is important to obtain a result that can be compared with the other numerical methods and analytical solution (for the sphere model case) to obtain comparable results. It is important to understand the behavior of plane wave inside the model, the mesh generation and how this impacts the modeling itself.

The mesh refinement, according to the wavelength, is a parameter that relates the element size in the mesh to the shortest wavelength, considering the fundamental relation:

$$\lambda_{FreeSpace} = \frac{c}{f} = \frac{3 \times 10^8}{f} \quad (41)$$

where f the frequency, c is the speed of the light, and $\lambda_{FreeSpace}$ is the wavelength in free space. Once $\lambda_{FreeSpace}$ is obtained, the maximum length of each patch or cell is taken as the eight or twelfth, even more depending on the local curvature of the bodies under considerations part of $\lambda_{FreeSpace}$, depending on the accuracy requirement. It is important to mention that in the case of a different material than free space, the wavelength will be reduced due to dielectric properties of material:

$$\lambda_{InsideMaterial} = \frac{\lambda_{FreeSpace}}{\sqrt{\epsilon_r}} \quad (42)$$

Equation (42) is taken into consideration for the volume-based methods, FEM and FIT, due to the full discretization of the body.

Also, related to bad results, the number of samples in the trajectories sometimes is important. It is not necessary to discretize very fine the number of elements to this AB and CD trajectories, but that is also proportional to the scale of the model and the required precision.

Another spotlight around on accuracy is the solution results with unphysical behaviors due to the solution not having a “good” and “smooth” functions and boundaries, or in the function itself. This is an indicator that the solution needs to be more precise.

This unnatural behavior can be a consequence of the CAD itself around the smoothness of the surface of the model. Remember that the computations of electric fields around corners is usually complicated and need more local mesh refinement. This problem appears when the surface itself is curved like in spheres and the ellipsoid cases. Also, this means that in the case of the approximation of the curve is bad, the result and boundary conditions will not be accomplished properly. To generate a smooth surface, it is necessary to increase the mesh as the following image, Figure 4.5, shows for spheres with different mesh refinements.

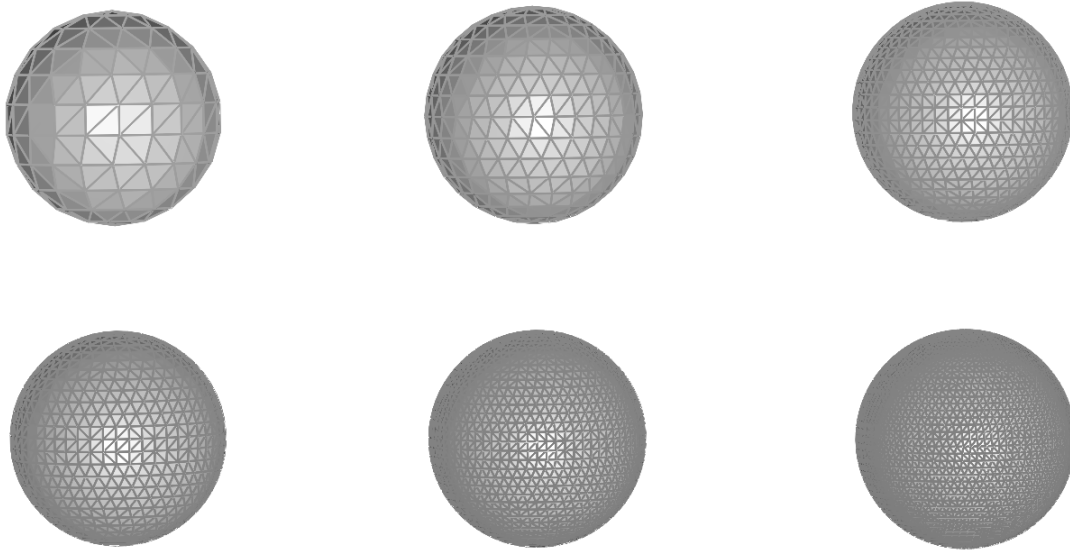


Figure 3. 5 Mesh quality. Is shown how the surface of the model changing due the variation of how many elements are required to describe the surface itself, is notable that in case of the increase of elements more smooth and accurate the surface will be generated

Also, a very good and detail mesh give a higher number of unknowns. The number of unknowns is proportional to the computation time and memory usage on the computer. }

3.7 Models Considerations with Regard to Specific Frameworks.

This chapter describes the development of the models in the three different codes. The first implementations developed are in Computer Simulation Technology (CST) [7], and High-Frequency Electromagnetic Field Simulation (HFSS) [8] which are both commercial tools and are based on FIT and FEM numerical techniques correspondingly; a third implementation was carried out in CONCEPT-II [9], an in-house tool at Hamburg University of Technology (TUHH) based on MoM.

The primary emphasis is to detail the requirements of the tools on the description of the geometric models and the generation of the mesh. As well as to the understanding of limitations that are presented for the obtaining of results comparable with each method and the available analytical solution.

3.7.1 CONCEPT-II Model Specifications.

CONCEPT-II code is based on MoM. The description of the mesh is a surface instead of a volume as described in Section 2.4.

In each case the setup of the geometrical model is similar, the full description will be presented just for the simplest model and then make highlights on the differences

with the ellipsoidal geometries. For example, the generation of the mesh and geometry, changes in code, etc. In Figure 3.6 is possible to see the direction of the plane wave (yellow) and the axis orientation (blue).

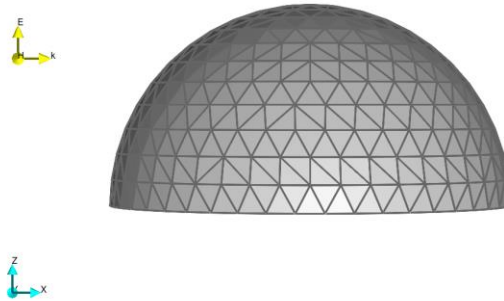


Figure 3. 6 Sphere model at 1 GHz of the generated model and mesh by CONCEPT-II CAD tool

In Figure 3.7, the angle of observation of the model has changed to see that is only a quarter of the overall sphere in simulation since symmetry planes were used in the simulation. The objective of doing so is to reduce the number of unknowns by a quarter of the original simulation and to complete model. This is also applied to the other codes to optimized the computational requirements.

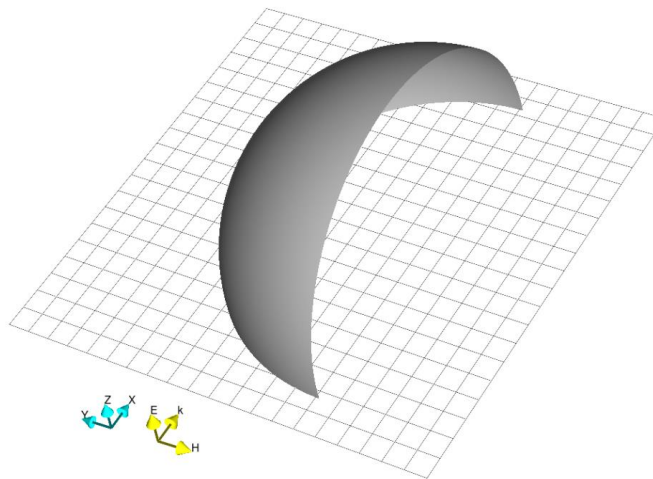


Figure 3. 7 The sphere model quarter in CONCEPT-II.

Figure 3.8 shows the CAD tool from CONCEPT-II. The discretization of the surface/mesh is one of the critical points in this kind of problems. The CAD tool gives the lambda refinement as “patches per wavelength.”

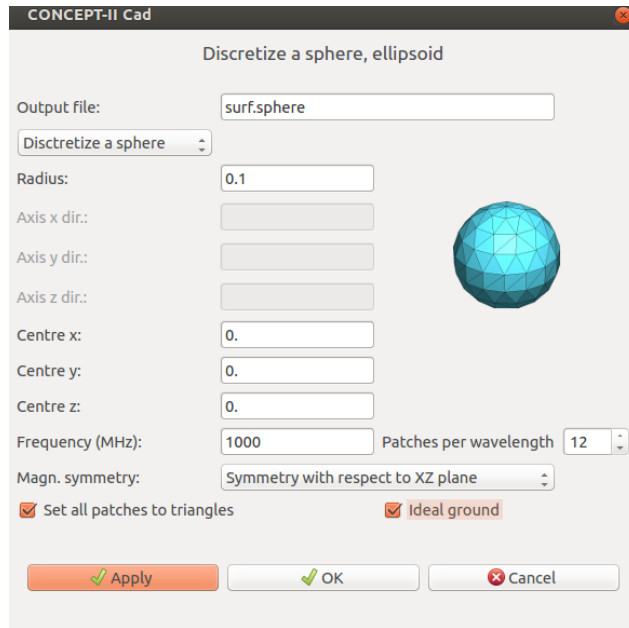


Figure 3. 8 Generation of the surface and mesh configuration.

At this point all the setup for other geometries is equivalent. It is valuable to mention that from Figure 3.6 and 3.8 these patches are set as triangles geometries to describe the surface. The Galarking matching method is used to obtain results with MoM.

One of the main requirements is the establishment and fulfillment of the boundary conditions. Because CONCEPT-II is a MoM based code, it is necessary that the tangential electric and magnetic field components at the surface and inside the model have to be equal at the boundary. Thus, the interface between water and air or free space, according to the fundamentals of electromagnetics, with this lossy material, is called dielectric boundary condition.

In general, the CONCEPT-II solver has numerous conditions, which are required to fulfill in order to obtain good results based on the fundamentals of physics. One of these conditions is a damping inside the body. In the particular case of the sphere model, the damping inside the body is lower than the electric field distribution obtains with the ellipsoidal geometries. This is due to the dimensions of the body and the number of patches required to have a good solution. To simulate the ellipsoidal models, the generation of the mesh was optimized due to the roughness of the mesh at the tips of the models and the possibility of elimination of the damping condition.

To finish this section, Table 3.3 shows a summary of all models and the number of unknowns required to get satisfactory results, capable of being compared with the solutions generated by the other tools.

Table 3. 3 Summary of CONCEPT-II simulations

| Software | Model | Frequency (GHz) | Number of unknowns | Time | Mem (GB) |
|------------|-----------------|-----------------|--------------------|----------|----------|
| CONCEPT-II | Sphere | 1 | 1028 | 00:00:05 | 0.016 |
| CONCEPT-II | | 2 | 1920 | 00:00:17 | 0.055 |
| CONCEPT-II | | 5 | 11966 | 00:02:27 | 2.133 |
| CONCEPT-II | | 7 | 23564 | 00:25:53 | 8.274 |
| CONCEPT-II | | 10 | 47466 | 01:05:32 | 34.378 |
| CONCEPT-II | Small Ellipsoid | 1 | 2318 | 00:00:15 | 0.08 |
| CONCEPT-II | | 2 | 7602 | 00:04:38 | 0.86 |
| CONCEPT-II | | 5 | 23306 | 00:35:37 | 8.09 |
| CONCEPT-II | | 7 | 27074 | 00:48:33 | 10.92 |
| CONCEPT-II | | 10 | 35802 | 01:31:02 | 19.1 |
| CONCEPT-II | Large Ellipsoid | 1 | 10990 | 00:17:50 | 1.80 |
| CONCEPT-II | | 3 | 38641 | 00:38:51 | 22.24 |
| CONCEPT-II | | 5 | 68558 | 03:06:40 | 70.03 |

3.7.2 CST Model Specifications.

Because in FIT and FEM based codes the definition of a 3D volume integration space is necessary, an open boundary condition and radiation boundary condition, respectively, are used in each tool to delimitate the computation region. The function of this bounding box is to delimit the integration space and neglect the reflections coming from that limits back to the objects within the model.

As a rule of thumb, this space should be located about $\frac{\lambda_{Freospace}}{4}$ away from the model, but other considerations during the development of the models showed that more distance is needed to get accurate and comparable results. Thus, it is appropriated to established greater bounding space to get better result to even $\lambda_{Freospace}$ or greater. As mentioned before, Figure 3.9 depicts an example of this definition of the bounding box around the model.

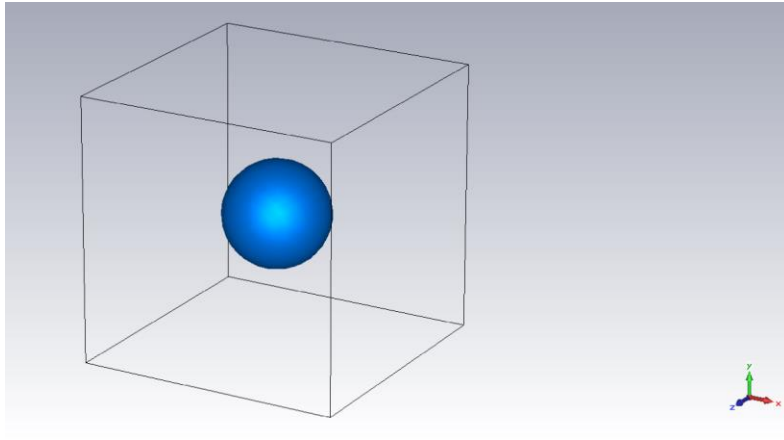


Figure 3. 9 Definition of the bounding box in CST

The next step is to set the boundary conditions at the box faces and the symmetry planes; here also the symmetry of planes is used to reduce memory consumption and computation time by simulating just a quarter of the model.

As mentioned earlier, the method used to discretize this model is more complicated than what the actual code shows (since the shifted mesh is not shown), but nevertheless is relevant to look at the mesh generated as shown in Figure 3.10.

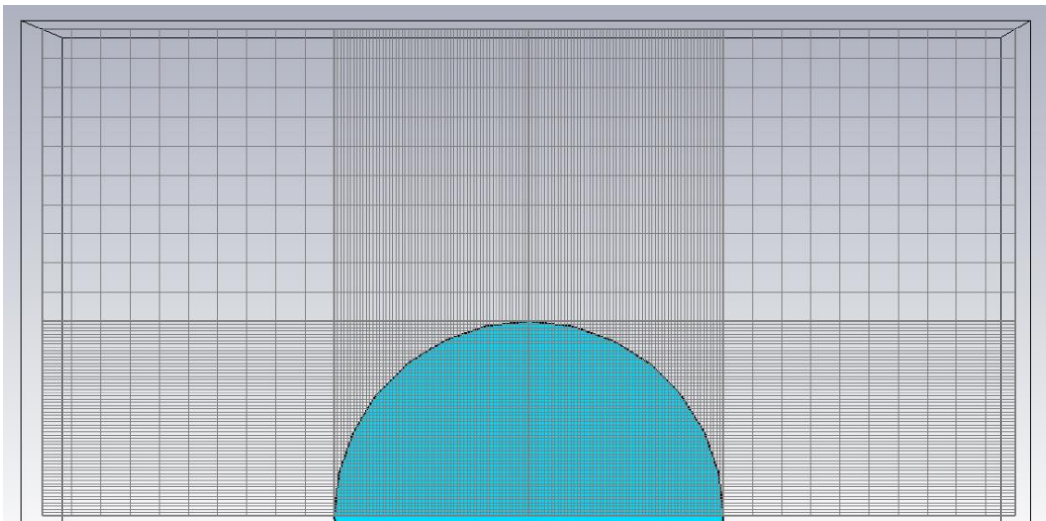


Figure 3. 10 Mesh plot generated by CST in the sphere model at 10 GHz

It is notable in Figure 3.10, that the mesh generated is “rough” or less detailed in the space between the sphere and the open boundary condition or the bounding box. This is expected because the E-field in free space needs fewer cells to be approximated because the definition of the refinement over the mesh is related to the size of the wavelength in free space the waves are larger. Closer to the model, it gets finer due to the smaller λ inside the model and at the body boundaries. Irregular boundaries from the geometrical perspective need more elements to

compute a precise solution. This occurs in the cases studied here smooth curvatures to the tips of ellipsoidal models and the sphere model. The solver and accuracy conditions selected are detailed in Figure 3.11.

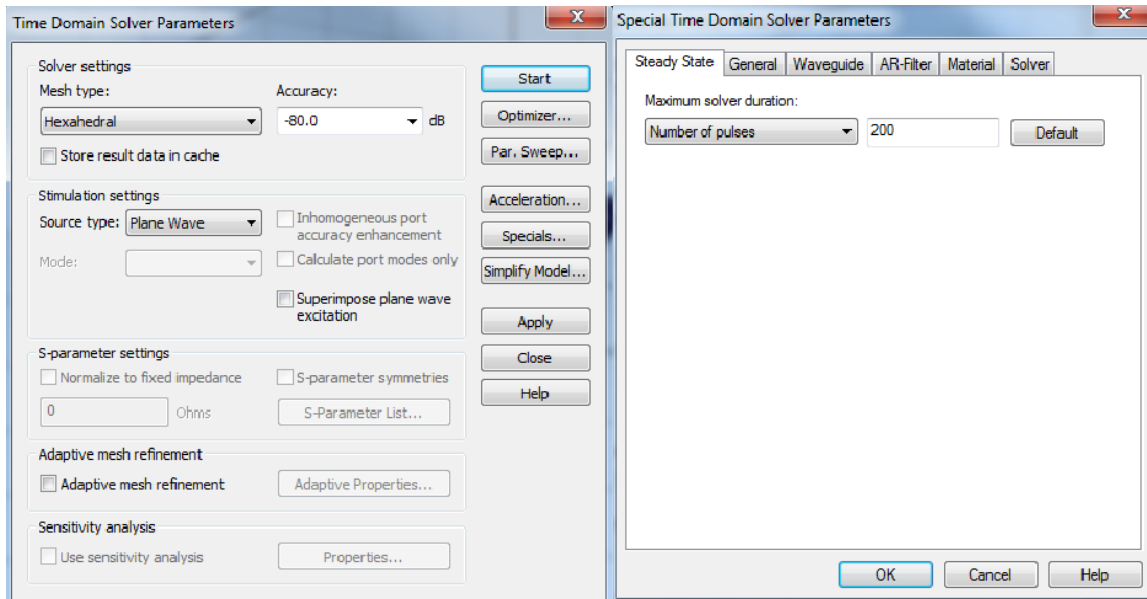


Figure 3. 11 CST Time domain solver set up

To finish this section a summary of all models developed with the CST MWS framework is shown in Table 3.4.

Table 3. 4 Summary of CST simulations

| Software | Model | Frequency (GHz) | Number cells | Comp Time | Memory (GB) |
|----------|-----------------|-----------------|--------------|-----------|--------------|
| CST | Sphere | 1 | 698 826 | 00:01:09 | .3077 |
| CST | | 2 | 1 608 714 | 00:14:07 | 1.533 |
| CST | | 5 | 31 049 568 | 02:53:41 | 12.305 |
| CST | | 7 | 52 396 146 | 06:44:32 | 25.069 |
| CST | | 10 | 66 772 496 | 14:10:29 | 31.737 |
| CST | Small Ellipsoid | 1 | 1 275 521 | 00:03:38 | .284 |
| CST | | 2 | 2 438 607 | 00:03:26 | .478 |
| CST | | 5 | 88 565 935 | 03:02:40 | 24.656 |
| CST | | 7 | 107 451 446 | 03:47:57 | 29.753 |
| CST | | 10 | 208 964 348 | 09:06:53 | 31.654 |
| CST | Large Ellipsoid | 1 | 47 394 200 | 01:40:29 | 13.284 |
| CST | | 3 | 185 558 145 | 05:36:35 | 31.677 |

3.7.3 HFSS model Specifications.

The boundary condition named “Radiation condition”, which resembles the open boundary condition was used. In HFSS, a PML boundary is also possible, but it would lead to a slower computation. The bounding box and the boundary condition can be observed in Figure 3.12 and Figure 3.13. In Figure 3.13, the mesh over the box is considered for the further comparison.

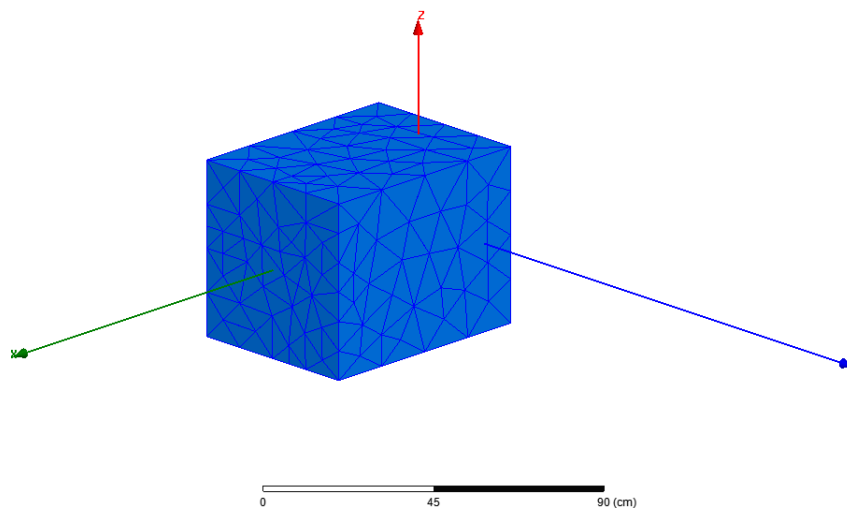


Figure 3.12 Mesh generated by HFSS in the bounding box at sphere model at 1 GHz

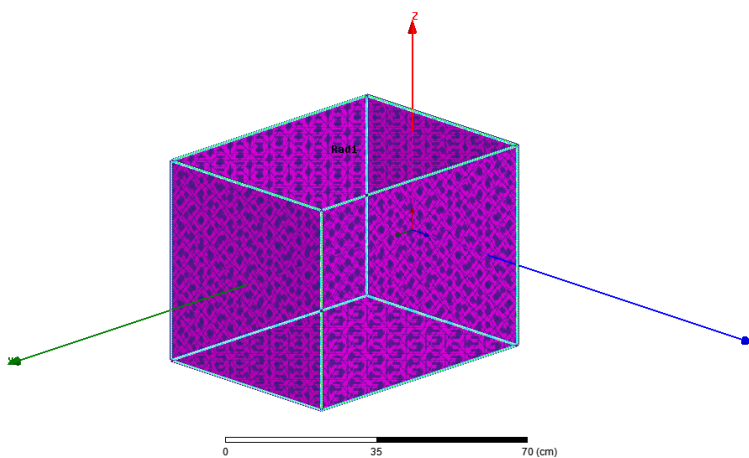


Figure 3.13 Boundary condition in HFSS at the bounding box at sphere model at 1 GHz

In Figure 3.14, the mesh inside the sphere is plotted. As in the previous case, the mesh is denser inside the body that outside due to a smaller wavelength and computational requirements over a lossy material.

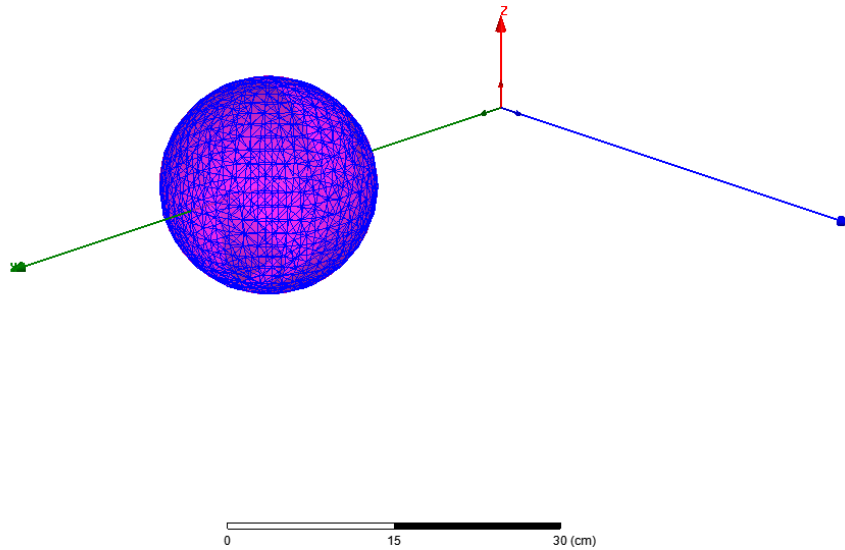


Figure 3. 14 Mesh generated by HFSS in the sphere model at 1 GHz

The field and in general the behavior of the analysis is from the total fields. As a default, HFSS shows in this kind of problems the scattered fields; this will lead to a different displayed result. This can be changed to match other solutions by editing the source display.

Figure 3.15 shows the solver setup for the sphere model at 1GHz. The frequency in analysis and the lambda refinement default settings are shown; this second point is important because the refinement is applied over all the integration space. This will lead to high memory consumption. Instead, the establishment of the local mesh refinement will provide better results. Also, the feature to increase the order of the basis functions and get more complex mesh generation features, and in general, better results can be traded off with the memory consumption.

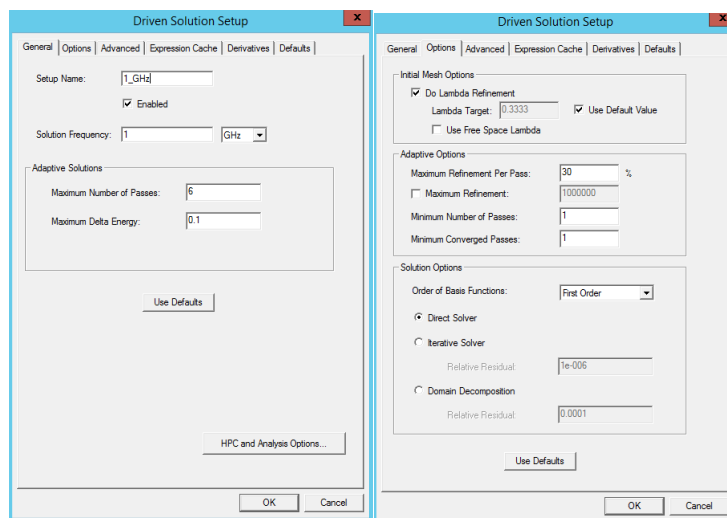


Figure 3. 15 Definition of the solver set up for the sphere model at 1 GHz

It is important to remark that HFSS use an interactive process to adapt the mesh and improve convergence (number of elements to describe the volume). Changing the conditions of Delta Mag Energy and the maximum number of passes, it is possible to get more accuracy increasing the simulation time and memory consumption.

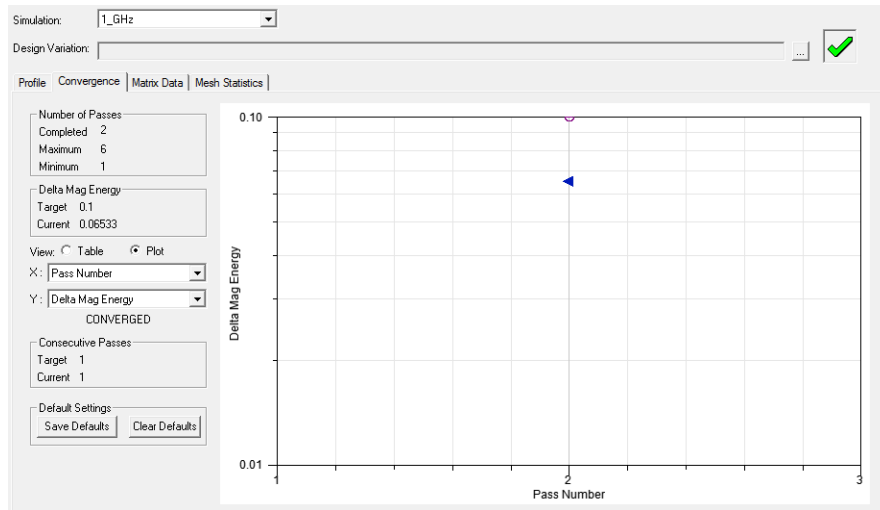


Figure 3. 16 Convergence and energy condition for the sphere at 1 GHz

Table 3.5 shows a summary of the model developed in HFSS. The main reason because the analysis could not be carried beyond 5 GHz was the hardware resources available. The simulation of the sphere at 5 GHz already consumes 40 GB of memory and provide inaccurate results in comparison to the other two tools. The results show non-natural behaviors when comes to the calculation over the CD trajectory. The main reason to explore the solution at 5 GHz is to established and demonstrate how the nature of the increasing number of elements is required to discretize and generated the model.

Table 3. 5 Summary of HFSS simulations

| Software | Model | Frequency (GHz) | Number of elements | Computation time | Memory usage (GB) |
|----------|--------|-----------------|--------------------|------------------|-------------------|
| HFSS | Sphere | 1 | 17873 | 00:00:51 | 1.010 |
| HFSS | | 2 | 69047 | 00:05:41 | 5.190 |
| HFSS | | 5 | 326563 | 01:35:28 | 40.900 |

The development of the SE and LE was done using the same techniques to minimize the number of unknowns. Some of procedures are: used of symmetry planes, local mesh conditions, general mesh conditions, optimize the solvers settings, more

complex basis functions, number of adaptive passes and generation by different means of the geometrical model (exported from CST and developed in HFSS), with no enough reduction of the complexity to be able to perform the analysis with the available resource.

4. Simulation Results with Regard to Electric Field Penetration

In this section, the comparison between the three numerical techniques implemented is presented in 3 different subsections divided by geometrical models. The results are presented from the lowest frequency models to the highest frequency ones.

The data is presented as the magnitude square of the electric field distributed along the surfaces of lines chosen for visualization. This quantity resembles, if scaled by the conductivity and density of the material, the point SAR.

As indicated before, the analytical solution used for the sphere can be found in [20]. This analytical solution is based on a summation of coefficients which have a finite precision. This is mentioned because, as is observed in section 4.1, the comparison in the values show a difference between the analytical solution and the others methods at certain frequency ranges.

The blue areas represent the outside region of the model, to remark where the boundary between the materials starts.

4.1 Sphere

4.1.1 Sphere Model Results at 1 GHz

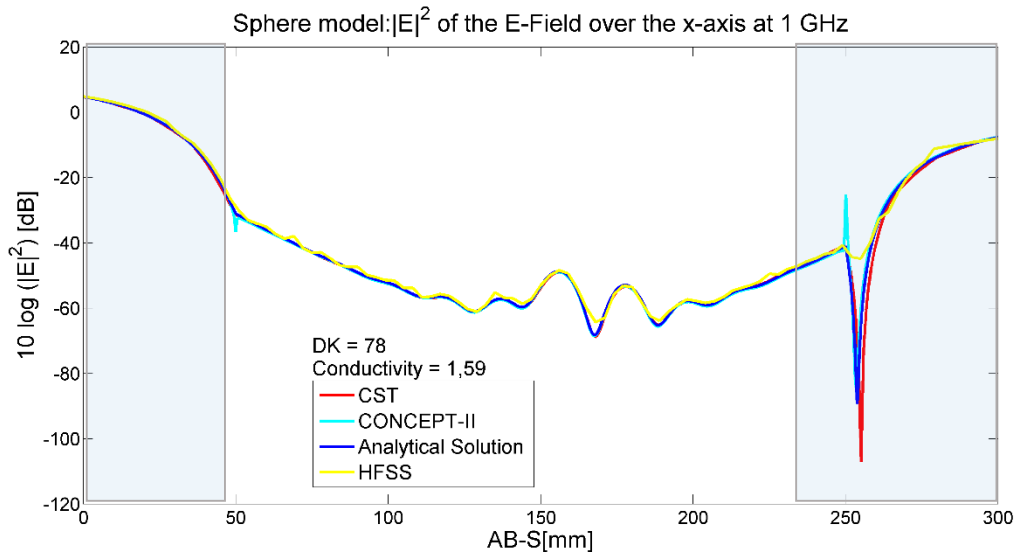


Figure 4. 1 S model: E^2 of the E_z -Field over the x -axis at 1 GHz

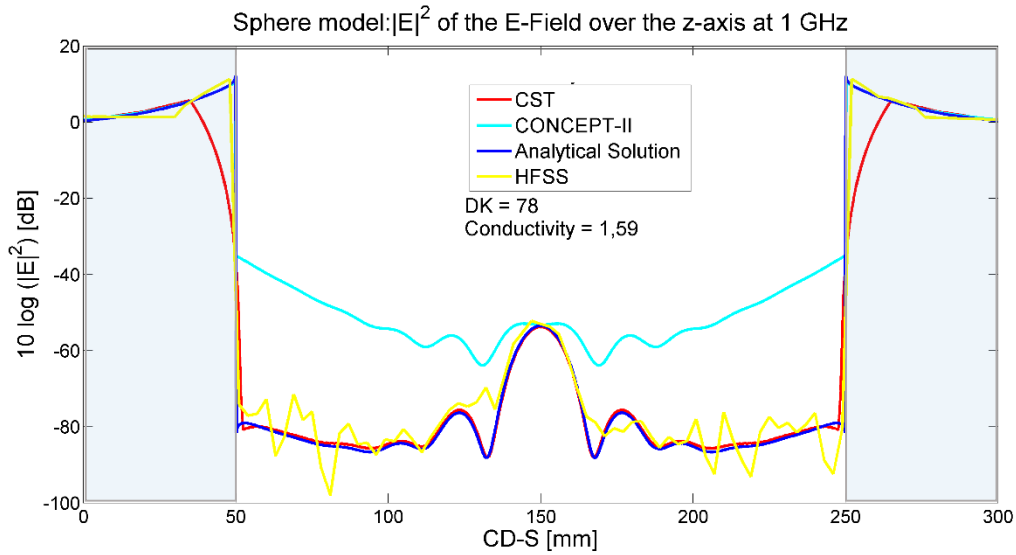


Figure 4. 2 S model: E^2 of the E_z -Field over the z -axis at 1 GHz

In Figure 4.1, a comparison of the results obtained at 1 GHz is shown, where a good agreement can be observed. In Figure 4.2, the results related to the sphere model and the trajectory CD have big differences with the analytical solution and two other methods. The reason for this is presumably the limitations of the available solution due to the computational resources available and the limitation of the analytical solution in terms of the coefficients to represent the values and the range of frequencies in the analysis. Note that the values showing differences for the CD trajectory are very small, and therefore the numerical noise floor in the methods might play a role.

The next figures are the results obtained for the sphere model at the highest computed frequency. Due to the considerations discussed in Section 3, related to the FEM based code, the results are not included in this document, since the solutions require further refinement.

4.1.2 Sphere Model Results at 10 GHz

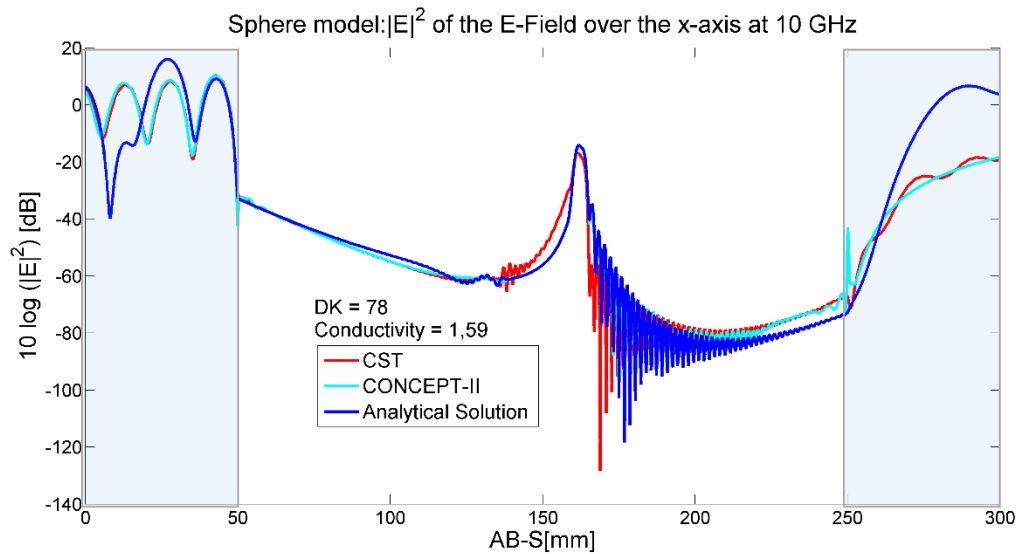


Figure 4. 3 S model: E^2 of the E-Field over the x-axis at 10 GHz

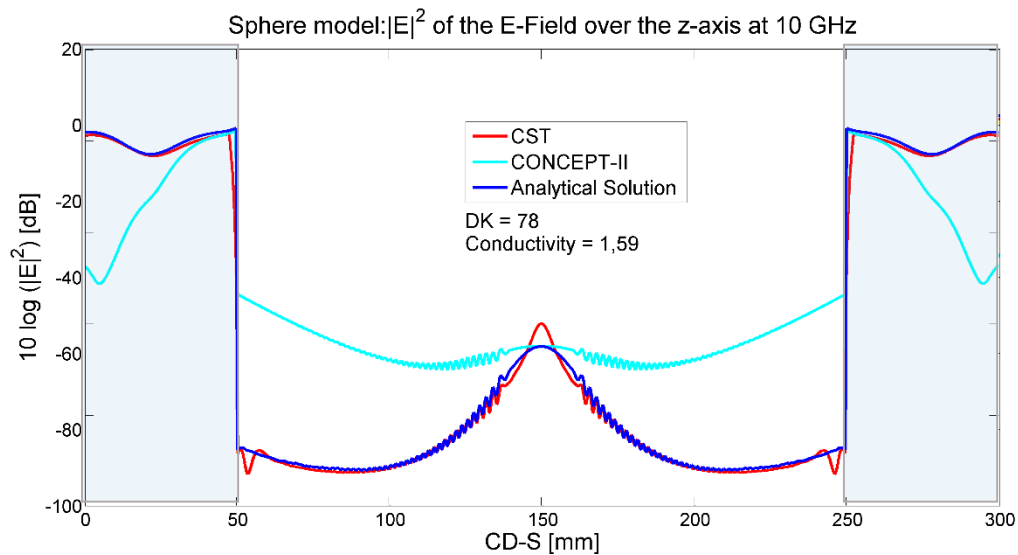


Figure 4. 4 S model: E^2 of the E-Field over the z-axis at 10 GHz

From Figure 4.3 and 4.4 and comparing the results obtained at 1 GHz, Figure 4.2 and 4.1, there are comparable numerical results between the codes and the analytical solution. This is notable over the AB trajectory, but over CD trajectory there are differences between codes. As before, this is attributed to the achievable precision required to estimate the values over the z-axis, due to numerical noise floor limitations.

4.2 Small Ellipsoid

From there, the comparison is limited to the FIT based code and MoM based code due to resource limitation discussed before. The increment of the body size represents significant differences in the electric field distributions. The changes in the results between codes is similar. The results are shown in Figures 5.5 to 5.8 for the small ellipsoid.

4.2.1 Small Ellipsoid Model Results at 1 GHz

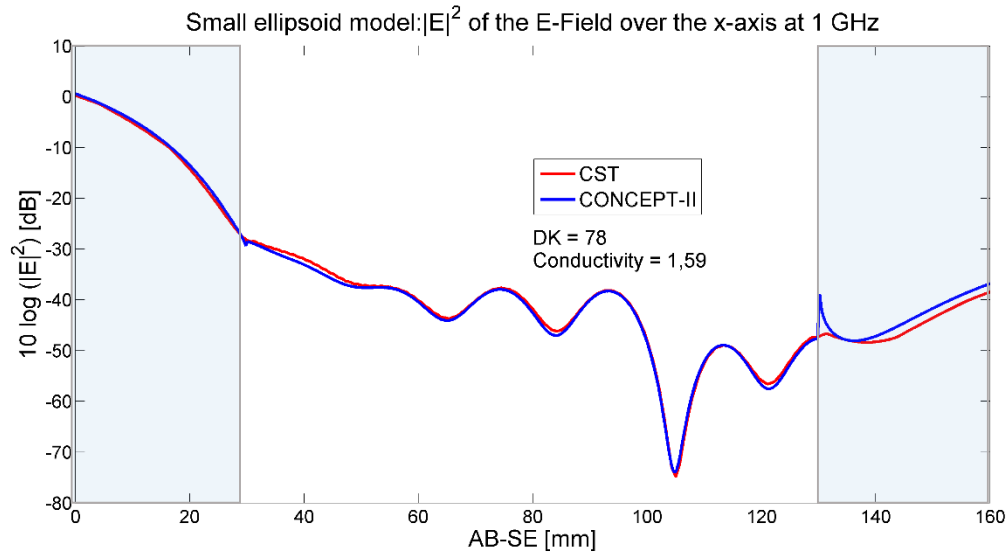


Figure 4. 5 SE model: E^2 of the E-Field over the x-axis at 1 GHz

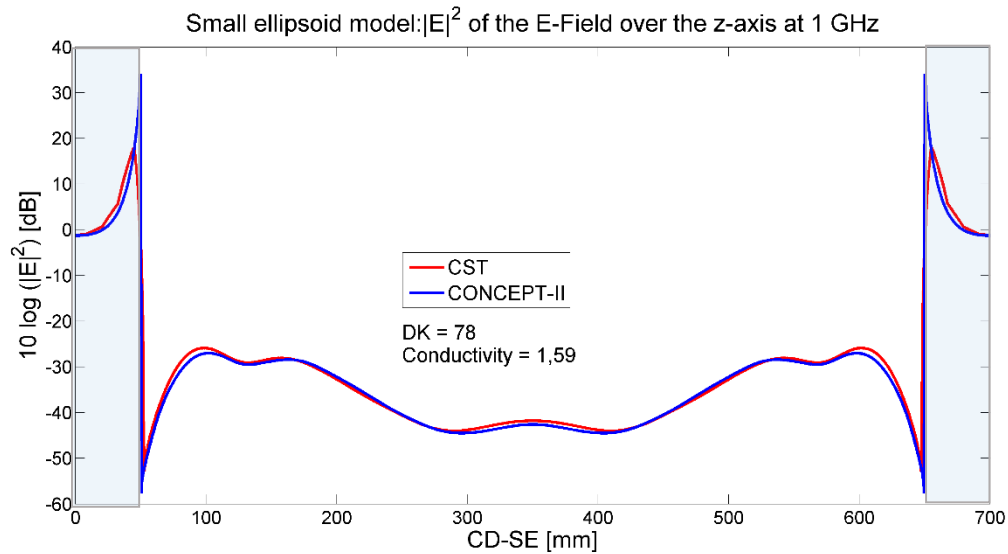


Figure 4. 6 SE model: E^2 of the E-Field over the z-axis at 1 GHz

The next section, 4.2.2, discusses the results for the ellipsoid at the highest frequency studied.

4.2.2 Small Ellipsoid Model Results at 10 GHz

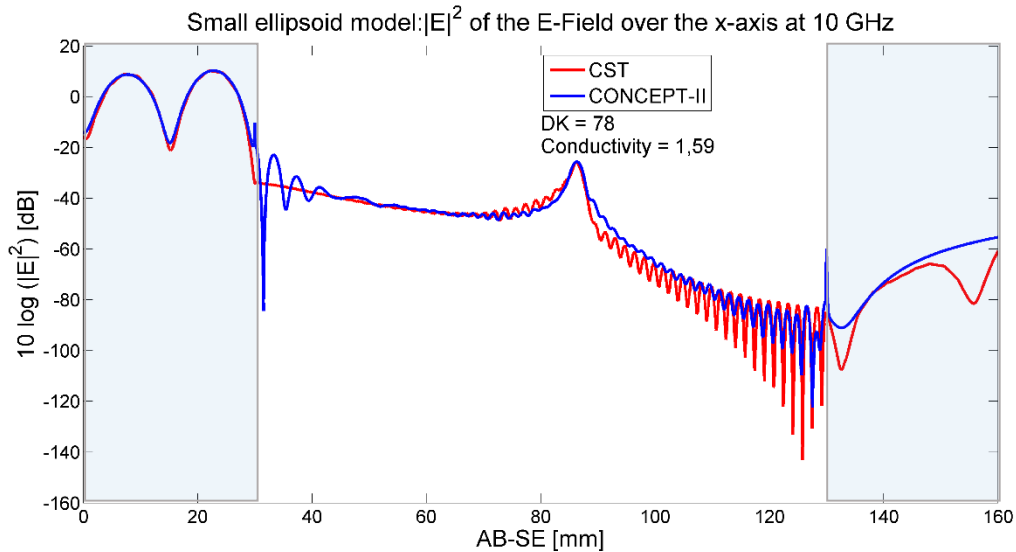


Figure 4. 7 SE model: E^2 of the E-Field over the x-axis at 10 GHz

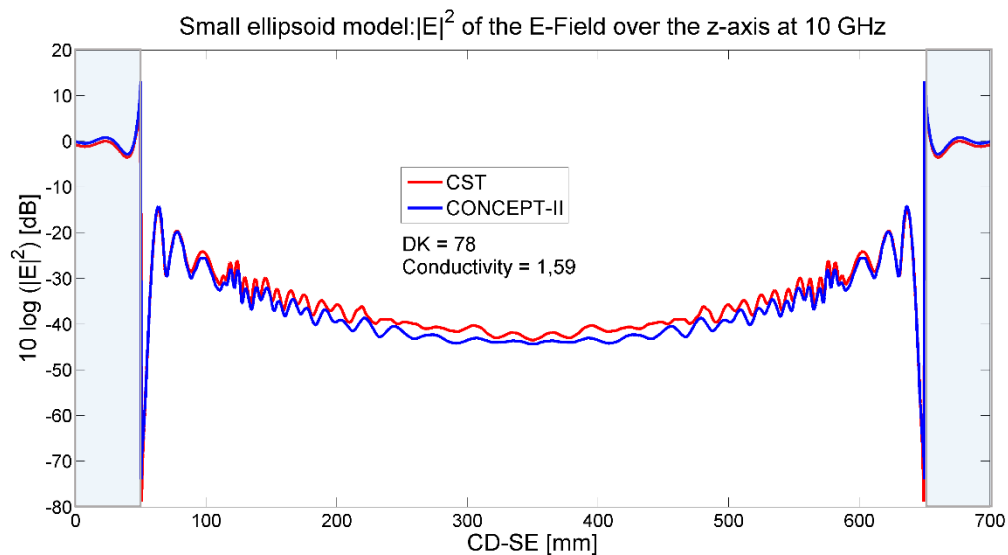


Figure 4. 8 SE model: E^2 of the E-Field over the z-axis at 10 GHz

There are more notable differences at the boundaries in the x-axis than in the z-axis. However the general trend is the same. The differences can be attributed to the

different grid over the evaluation line that given the rapid variations, might lead to differences on the interpolation.

4.3 Large Ellipsoid

The large ellipsoid model has dimensions that are comparable to the size of an adult human body. From Figure 4.9 to 4.12 the results are compared between CST and CONCEPT-II due to the large size of this model, the highest analyzed frequency is 3 GHz.

In comparison to the results obtained for other geometries, the damping inside the bodies is greater, and the resonant behavior inside the structure shows different patterns and a lower level for the field concentration peak at the central region.

4.3.1 Large Ellipsoid Model Results at 1 GHz

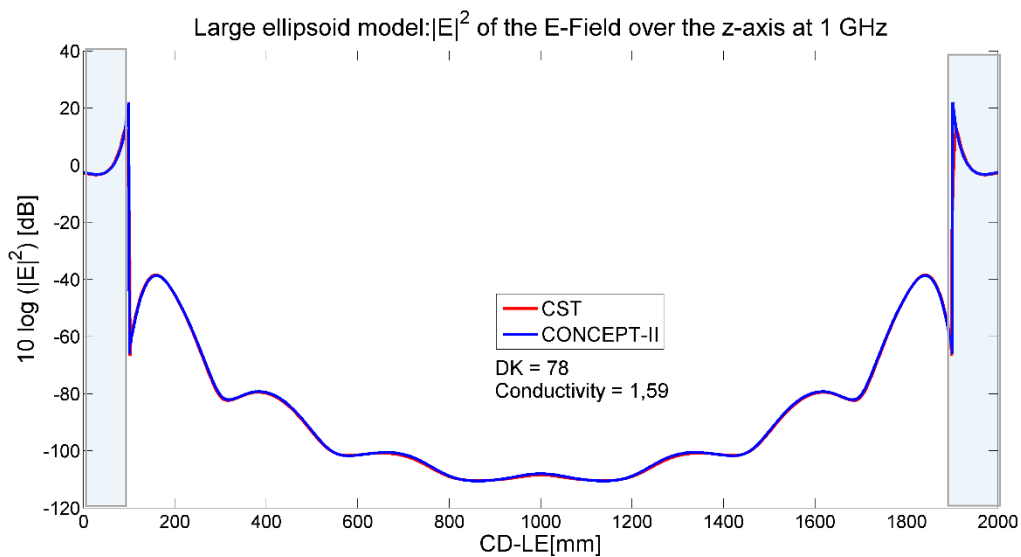


Figure 4. 9 LE model: E^2 of the E-Field over the z-axis at 1 GHz

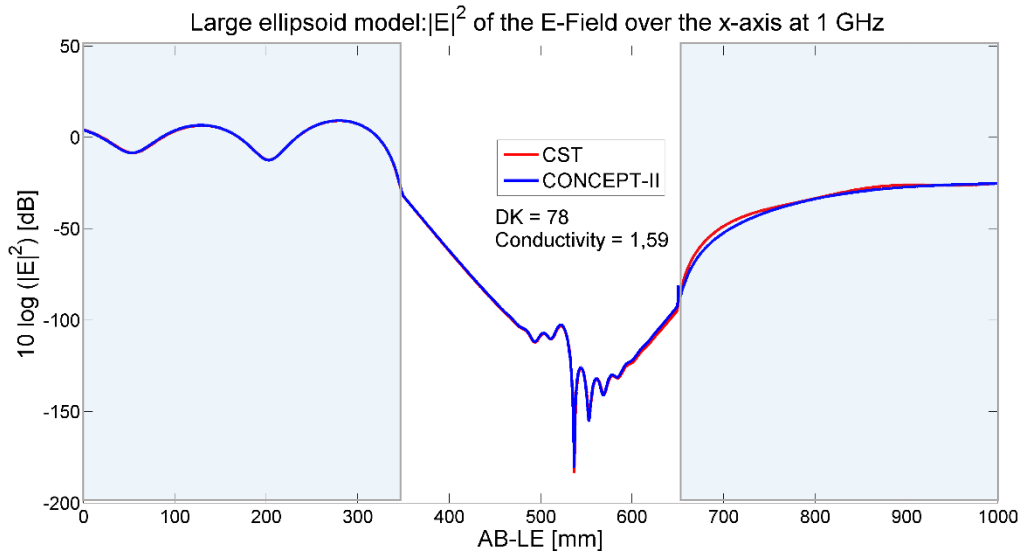


Figure 4. 10 LE model: E^2 of the E-Field over the z-axis at 1 GHz

As in other cases, the comparison at 1 GHz shows similar results; the boundary conditions are consistent among methods. There are some small differences at 650 mm, which are attributed to the superposition of the inside wave patterns and the outside wave patterns, also due to the different wave velocities of propagation. This approximation is difficult because of the complex field behavior mentioned before.

4.3.2 Large Ellipsoid Model Results at 3 GHz

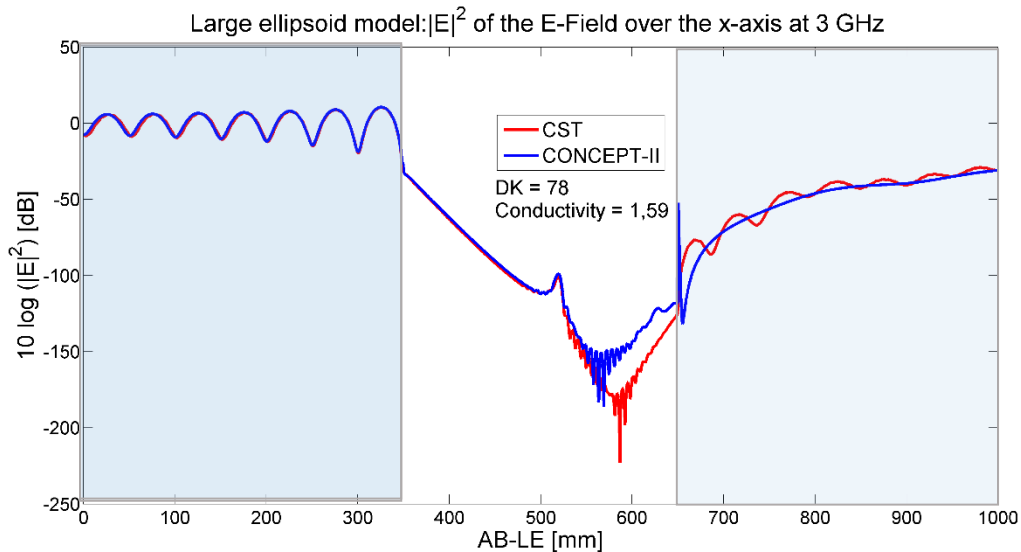


Figure 4. 11 LE model: E^2 of the E-Field over the x-axis at 3 GHz

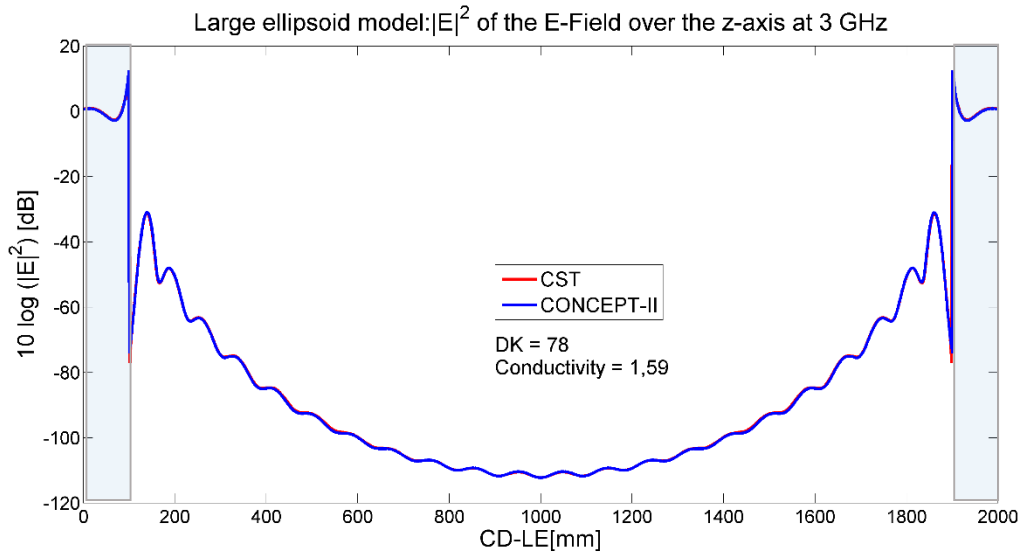


Figure 4. 12 LE model: E^2 of the E-Field over the z-axis at 3 GHz

As a summary, the agreement of all models implemented in the three tools gave comparable good result up to 2 GHz in the AB trajectory. But at 5 GHz, FEM based code gave bad results with the sphere model in comparison to the other two techniques and the analytical solution, presumably due to the insufficient refinement of the numerical solution due to a lack of computational resources.

This is attributed to the nature of the numerical technique being an iterative method expensive regarding computational requirements. To calculate the values of the sphere model request about ten times more memory consumption for the FEM solver in comparison to the other two codes. This results in a much larger computational requirement demand when comes to electrically large structures and small values inside the geometry.

From the variation of frequency up to 10 GHz for the S and SE models and up to 5 GHz from LE model over the CD trajectory, it is relevant to remark that the damping of the E-Field inside the model in every frequency rapidly increases.

Also, it is relevant to observe that with the increase of frequency in every model there is a greater concentration of E-Field at the boundary where the plane wave is illuminating.

5. Simulation Results

5.1 Simulation Results with Regard to Field Behavior

This section is devoted to discussing the validation of the solutions based on the understanding of physics of the field behavior with the interface between free space and water from 2D plots.

This section highlights the main observations and analysis that give in conclusion the validation of the 2D plots according to electromagnetics fundamentals such as plane wave behavior and boundary conditions. Also, it is relevant to exposed that the solutions and plots shown are just from CONCEPT-II because the numerical correspondence between techniques already has been addressed in section 5.

In Figures 5.1 and 5.2, a comparison of the effect of increasing the frequency for the sphere model is illustrated. It is possible to see that the electric field behavior outside the model is quite different; note that different wavelengths are associated. Also, the wavelength related maximum and minima of the plane wave surrounding the sphere can be seen. The higher intensity spots, in red and yellow along the outer circumference, are more distant in Figure 2 in comparison to Figure 3, which is the result of a longer outside wavelength at 1 GHz. The figures also show the field contrast between the inner region of the sphere and outer free space region at 1 GHz and 10 GHz, each for a phase of 0 degrees. It can be observed that although the strong damping in both cases, at 1 GHz still some fields are observed inside the sphere in the linear scale shown. This is not possible anymore with the linear scale at 10 GHz. Vortices inside the sphere and more intense circular fields at the center of the body are predicted by the analytical solution as well. These phenomena appear due to a superposition effect inside the body.

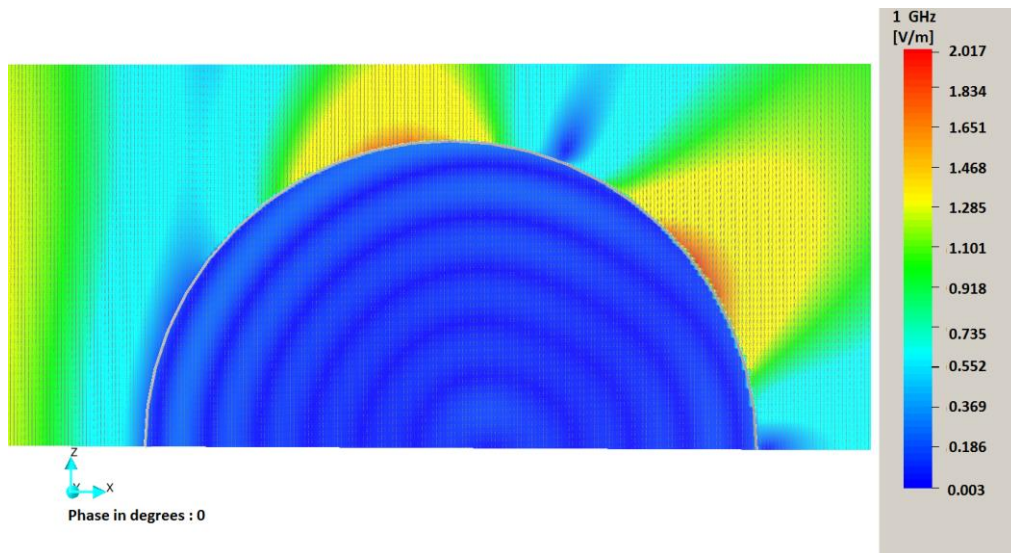


Figure 5. 1 XZ plane, E-field behavior for the sphere model at 1 GHz

Through Figure 5.2, it is possible to notice the behavior of the E-field pattern along the circumference of the sphere is changing. In this case, the model is solved up to 10 GHz, which means that the wavelengths in free space are shorter than at 1 GHz.

Taking into consideration the wavelength size and the reflection of the plane wave, the result of the wave pattern behavior observable in the 5.2 Also, this behavior of the plane waves is highlighted in Figure 5.3 with the larger scale of small values inside the sphere, red color arrows, and the wave pattern behavior of maximum and minimum peaks indicates the superposition of waves due to the reflection.

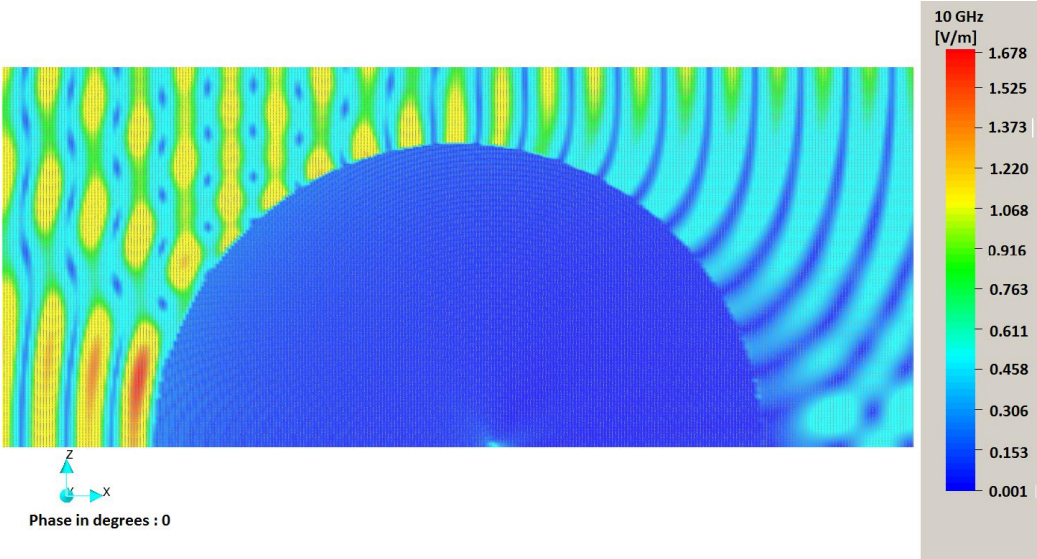


Figure 5. 2 XZ plane field behavior sphere model at 10 GHz

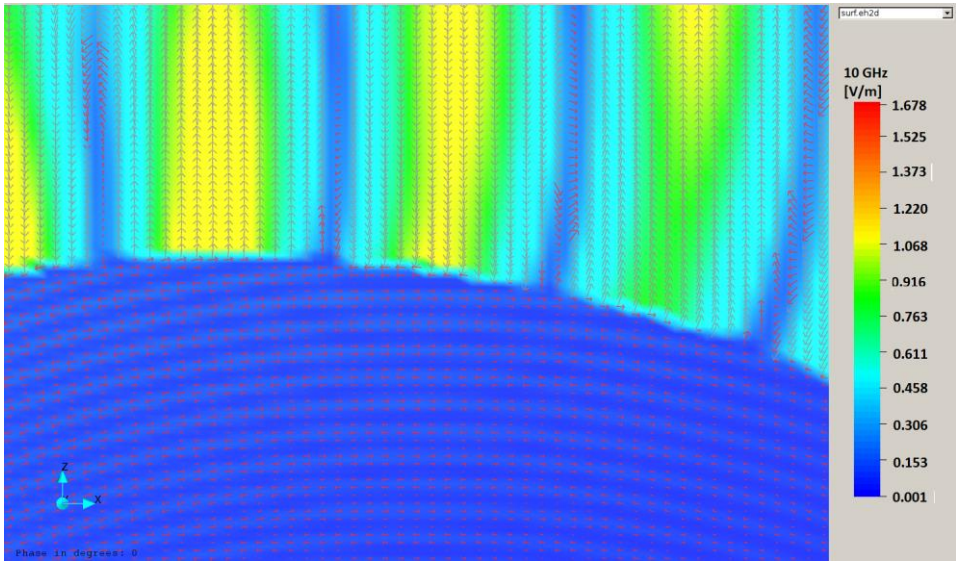


Figure 5. 3 XZ plane E-field behavior sphere model at 10 GHz zoom and visualization of small values (red arrows)

Also, it is important to notice the difference with the scale of the model size itself. In Figure 5.2 shows the exact same configuration than Figure 5.4, but changing the geometry of the model to the small ellipsoid. The resonance is still in the middle of the model, along with the z-axis, and even an increase of the concentration of E-field at the tip of the model due to the reduction of the overall distance and the superposition of traveling waves. A similar phenomenon as in the case of the sphere.

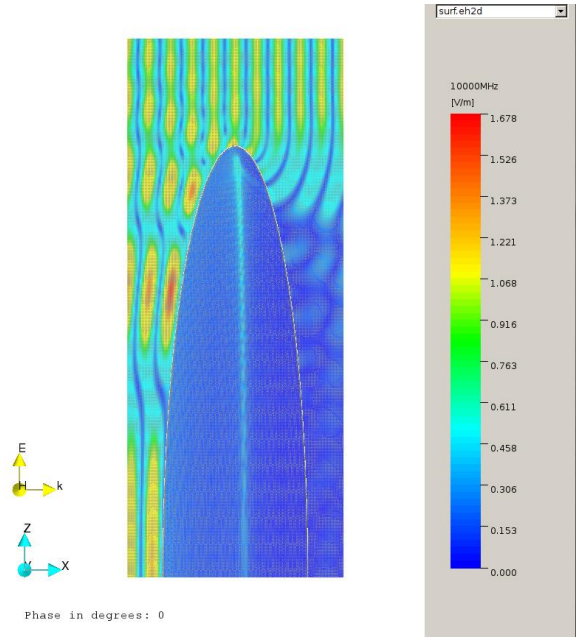


Figure 5. 4 XZ plane E-field behavior small ellipsoid model at 10 GHz

In Figure 5.5 is plot the same configuration but scale the model to the large ellipsoid at 1GHz. The pattern is different mainly because of the apparent reduction of the resonance at the middle of the body; this is remarked in the results shown in Section 4. This effect is due to the enlargement of the radius of the model and also according to [2] to the resonance of the body itself. The resonance has a direct relationship to the dimensions of the body.

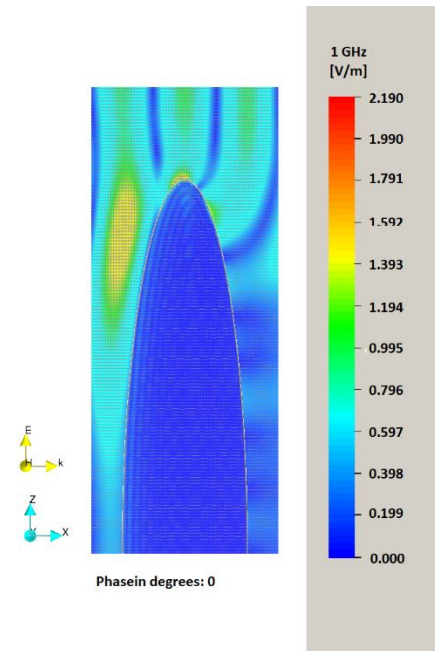


Figure 5.5 XZ plane E-field behavior large ellipsoid model at 1 GHz

From the large ellipsoid model, it is possible to get even more results creating a specific fine plot in the area where the plane wave is directly hitting the body. The configuration shown in Figure 5.6 is the general sketch to reference the results in Figures 5.7 and 5.8.

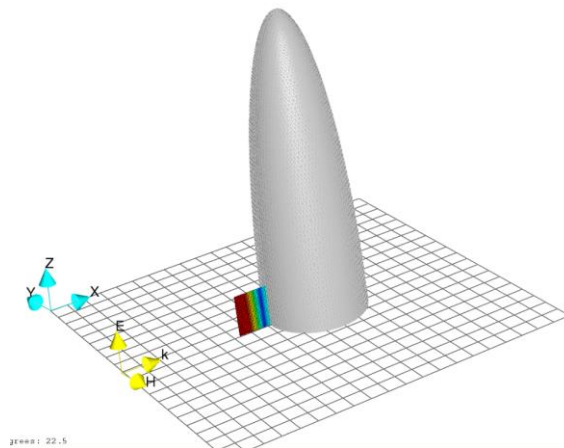


Figure 5.6 Configuration to plot the behavior at a specific area of the large ellipsoid at 1 GHz

In Figure 5.7 is notable the wave pattern from the incident and reflected plane wave. Also, the penetrating fields show how the overall traveling waves inside the body decay very rapidly.

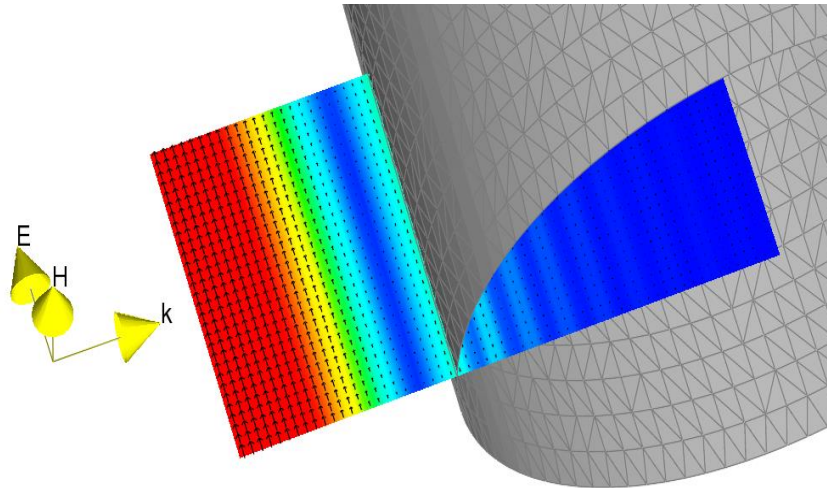


Figure 5.7 Plot xz plane for the setup shown in Figure 5.6 as a close up to the plot.

In Figure 5.8, the fulfillment of the boundary condition $E_{T1} = E_{T2}$ is shown.

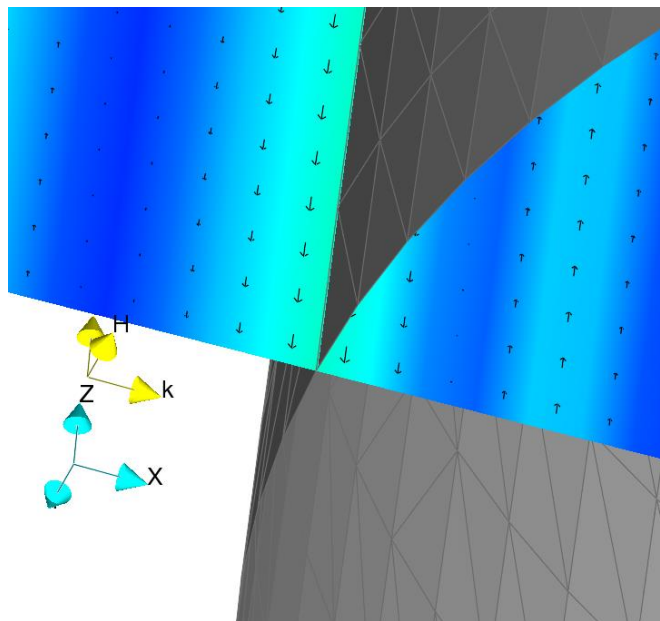


Figure 5.8 Plot xz plane for the setup shown in Figure 5.6 as a detail to observe boundary conditions.

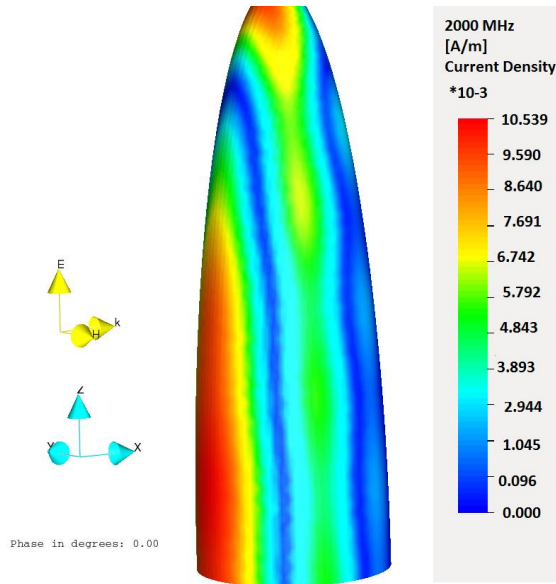


Figure 5.9 Current distribution for the LE at 2 GHz

From Figure 5.9, it is possible to see the current distribution over the LE model. It is notable that almost all field is distributed over the front face of the model, which is the part that is being illuminated by the plane wave excitation. This energy is mostly at the surface of the body itself.

From Figure 5.1, Figure 5.2 and 5.7, it is possible to see, especially in figure 5.7, the wave pattern at the outside. This is evidence of the “bad conductor” behavior expected for the studied material and geometries.

5.2 Comparison of Computational Effort

In the following table, there is a summary of simulation execution regarding frequency, memory usage or consumption, and computation time. The main reason for not including terms related to mesh requirements and matrix size is because of the differences between each numerical technique and the approach to generate the mesh.

Table 5. 1 Comparison of the computational resources necessary for all used tools

| Software | Model | Frequency (GHz) | Number of elements | Comp Time | Memory (GB) | |
|----------|-----------------|-----------------|--------------------|-----------|--------------|------|
| FIT | Sphere | 1 | 698 296 | 00:01:09 | .308 | |
| | | 2 | 1 608 714 | 00:14:07 | 1.533 | |
| | | 5 | 31 049 568 | 02:53:41 | 12.305 | |
| | | 7 | 52 396 146 | 06:44:32 | 25.070 | |
| | | 10 | 66 772 496 | 14:10:29 | 31.737 | |
| MoM | | 1 | 1028 | 00:00:05 | 0.016 | |
| | | 2 | 1920 | 00:00:17 | 0.055 | |
| | | 5 | 11 966 | 00:02:27 | 2.133 | |
| | | 7 | 23 564 | 00:25:53 | 8.274 | |
| | | 10 | 47 466 | 01:05:32 | 34.378 | |
| FEM | | 1 | 17 873 | 00:00:51 | 1.010 | |
| | | 2 | 69 047 | 00:05:41 | 9.920 | |
| | | 5 | 326 563 | 01:30:00 | 40.900 | |
| FIT | | Small Ellipsoid | 1 | 1 275 521 | 00:03:38 | .284 |
| | | | 2 | 2 438 607 | 00:03:26 | .478 |
| | 5 | | 88 565 935 | 03:02:40 | 24.656 | |
| | 7 | | 107 451 446 | 03:47:57 | 29.753 | |
| | 10 | | 208 964 348 | 09:06:53 | 31.654 | |
| MoM | 1 | | 2 318 | 00:00:15 | 0.080 | |
| | 2 | | 7 602 | 00:04:38 | 0.860 | |
| | 5 | | 23 306 | 00:35:37 | 8.090 | |
| | 7 | | 27 074 | 00:48:33 | 10.290 | |
| | 10 | | 35 802 | 01:31:02 | 19.100 | |
| FIT | Large Ellipsoid | 1 | 47 394 200 | 01:40:29 | 13.284 | |
| | | 3 | 185 558 145 | 05:36:35 | 31.677 | |
| MoM | | 1 | 10 990 | 00:17:50 | 1.800 | |
| | | 3 | 38 641 | 00:38:51 | 22.240 | |
| | | 5 | 68 558 | 03:06:40 | 70.030 | |

The final results obtained for the computational comparison, Table 5.1, and from Figure 5.10 to Figure 5.15 show that the resources required by FIT and FEM are higher in comparison to MOM, with simulation times longer by up to ten times. This is because of the requirement of the mesh generation and the number of elements required to describe the model.

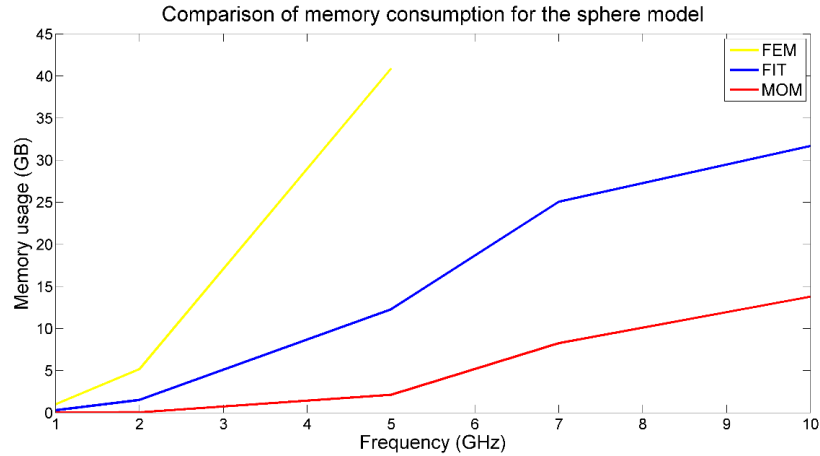


Figure 5. 10 Comparison of the memory consumption for the sphere model

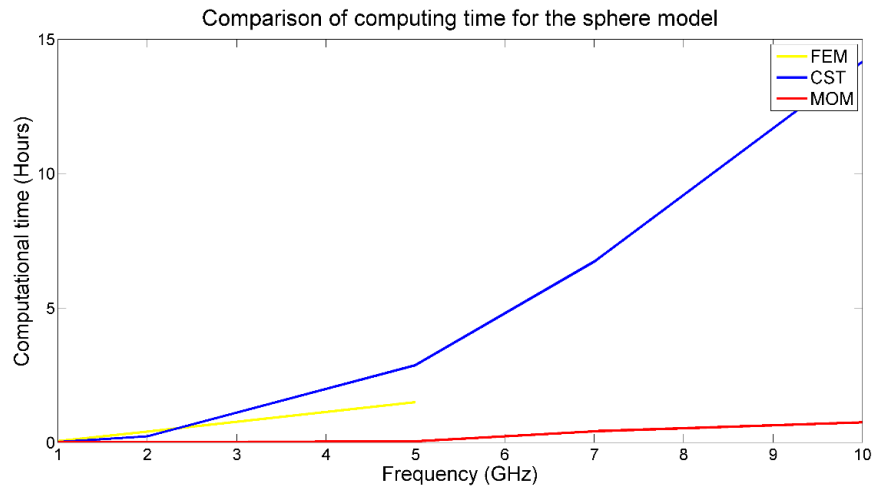


Figure 5. 11 Comparison of computing time for the sphere model

Figure 5.10 and 5.11 shows the difference between codes about computational resources for the sphere geometry. MoM shows better results in the management of memory and time to obtain a comparable to FEM and FIT based codes. This behavior is expected due to the discretization of the mesh required for a surface-based method compared to the volume method and the need to define a bounding box to delimit the integration space.

Also, it is important to remark the behavior through the frequency of the codes. The number of unknowns grows difference depending on the method. A volume base method shows a nearly cubic increasing behavior in the number of unknowns and surface based methods shows more a quadric relationship.

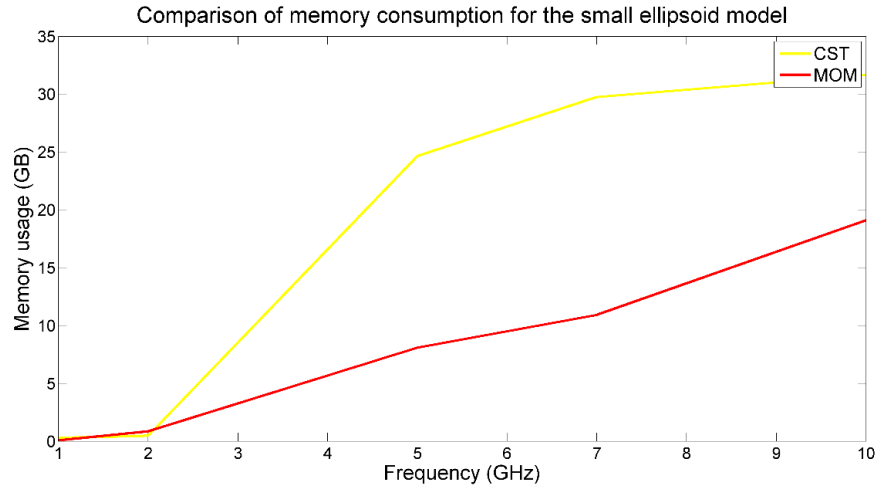


Figure 5.12 Comparison of the memory consumption for the small ellipsoid model

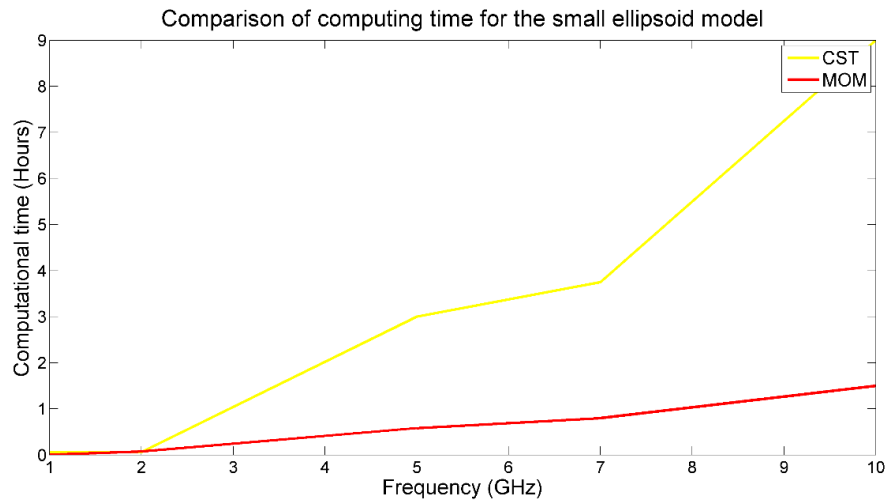


Figure 5.13 Comparison of computing time for the small ellipsoid model

Figure 5.12 and 5.13 the comparison between the small ellipsoid geometrical models computational resources for each code. Comparing the behavior of the sphere and ellipsoid, the last shows similar approximations related to computational effort and the time required to obtain comparable numerical results.

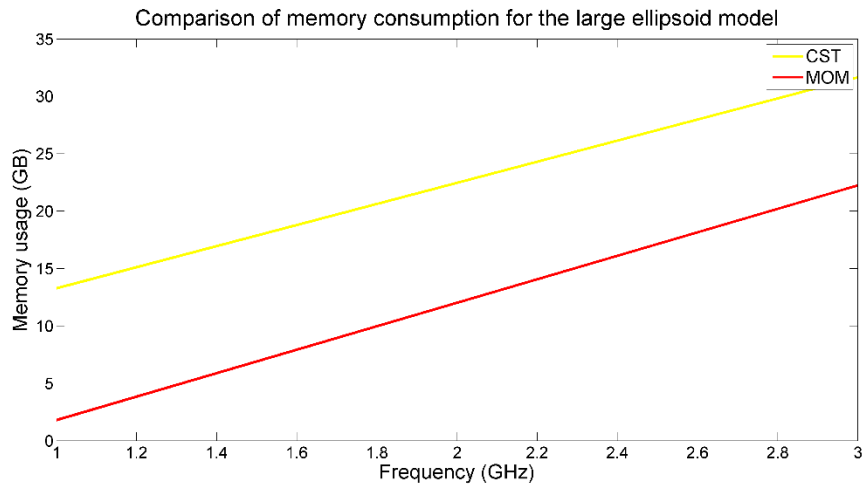


Figure 5. 14 Comparison of the memory consumption for the large ellipsoid model

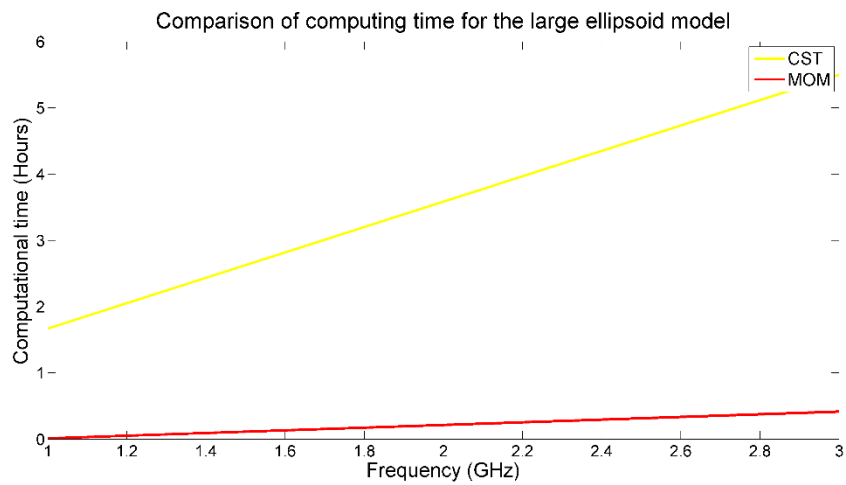


Figure 5. 15 Comparison of computing time for the large ellipsoid model

It is also notable from Table 5.1 that the number of unknowns to describe the mesh for each model is increasing the size of the models and the complexity of each geometry. It is relevant to take into consideration that volume methods require higher mesh density because of the model itself and the bounding box necessary for the volume method to generated results. MOM itself shows equally better results as the others in less time and with less computational effort, although at higher frequencies this advantage is not clear anymore.

The results and experiments were done indicate that it might be possible to use an approximation with a surface model for many situations due to the huge damping inside the body and limited field penetration in the GHz range.

5.3 Comparison of Electric Field Penetration and Variation of the Material Conductivity

In the following Figures, 5.16 to 5.19, it is possible to see the frequency behavior of the models from the sphere to the large ellipsoid. These results are from CONCEPT-II only:

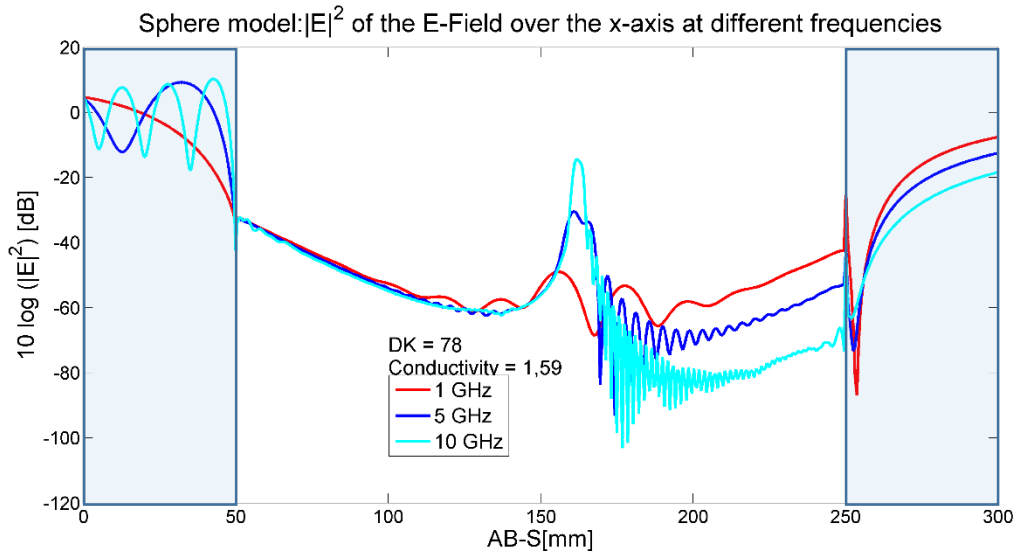


Figure 5. 16 S model: Magnitude of the Ez-Field over the x-axis at different frequencies

In Figure 5.16 the comparison through the frequency of the electric field behavior for the sphere model is shown. As remarks, the most notable behavior is the superposition of the electric field inside the geometry, and the standing wave like behavior on the illuminated area due to the plane wave incidence. This is the only geometry that shows this increase with frequency at the center of the model, presumably due to the symmetry of the model.

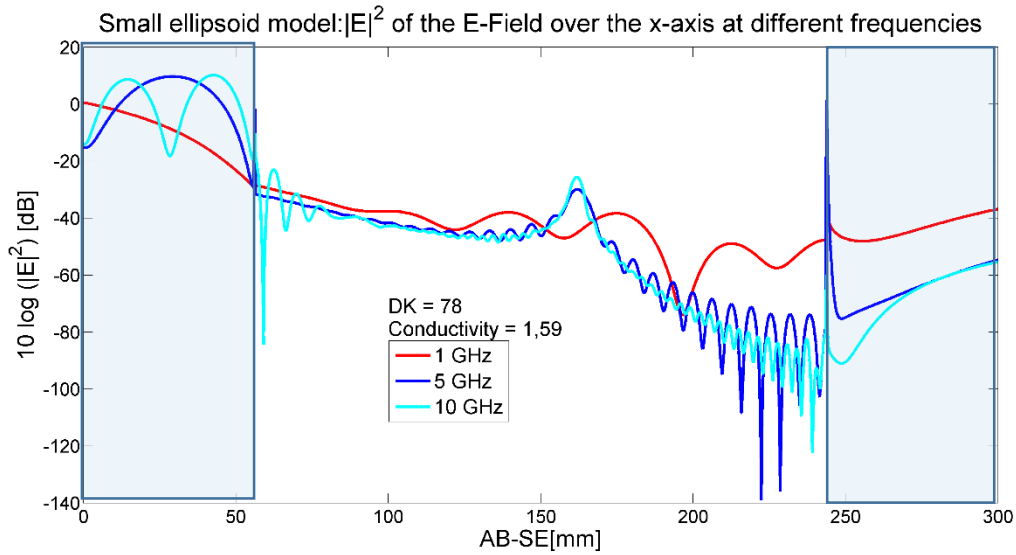


Figure 5.17 SE model: Magnitude of the E_z -Field over the x-axis at different frequencies

In Figure 5.17, the comparison through the frequency of the electric field behavior for the small ellipsoid model is shown. In comparison to the behavior of the sphere model, the resonant demeanor is almost non-variable for the 5 GHz and the 10 GHz frequencies. For the 1 GHz solution, there is a difference in the electric field pattern; this is due to the size of the wavelengths compare to the object and the field superposition on the structure.

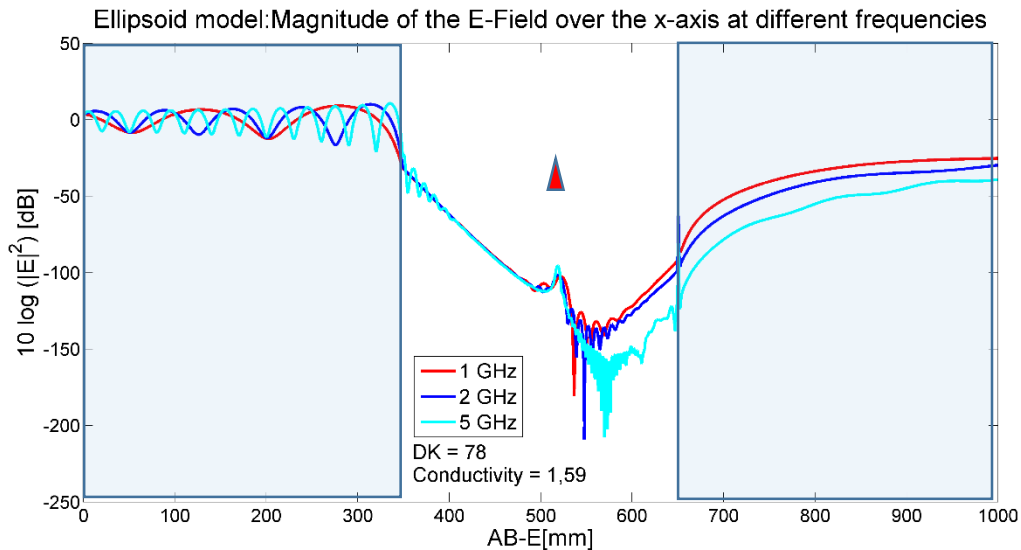


Figure 5.18 LE model: Magnitude of the E_z -Field over the x-axis at different frequencies

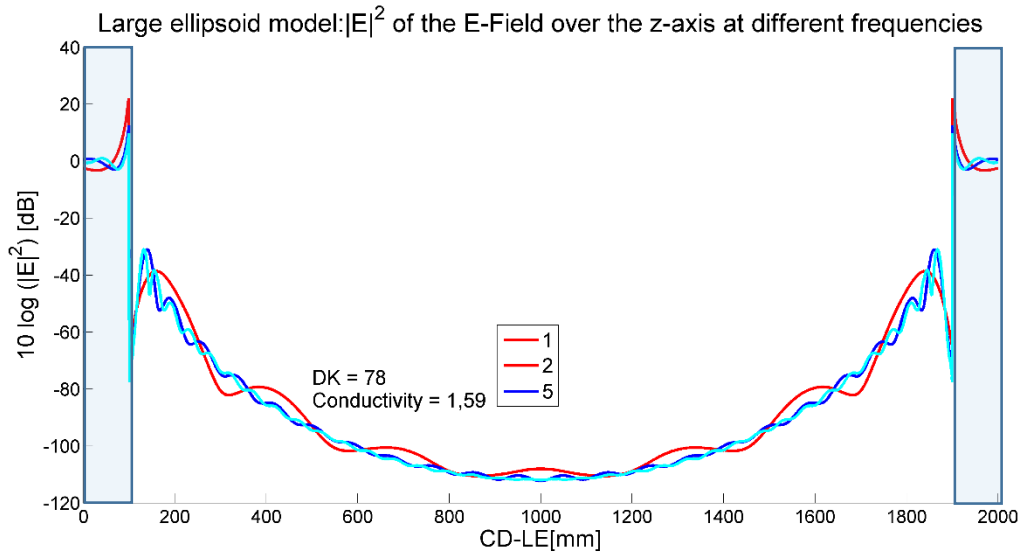


Figure 5. 19 LE model: Magnitude of the Ez-Field over the z-axis at different frequencies

It is also relevant to see the effect of frequency on the models, which can be seen from Figure 5.17 to 5.19.

The scale of the models and the increase of z dimension in each model: 30 cm, 70 cm, and 180 cm, respectively sphere, small ellipsoid and large ellipsoid, is associated with a power concentration in the middle area of the bodies, decreasing the size of the model.

The reason for this concentration is attributed to the superposition of waves. The effect is stronger for the S and SE models, but in the LE model, it is less accentuated with values as low as -100 dB. In Figure 6.18, it is possible to compare this peak value inside the large ellipsoid model to the red triangle, which resembles the range in which the peak values of the sphere and small ellipsoid geometries are.

Figure 6.20 and 6.21 are made considering the frequency dependency of water and the tendency of increasing conductivity over frequency. In Figure 6.20 is for AB trajectory and Figure 6.21 for the OD trajectory

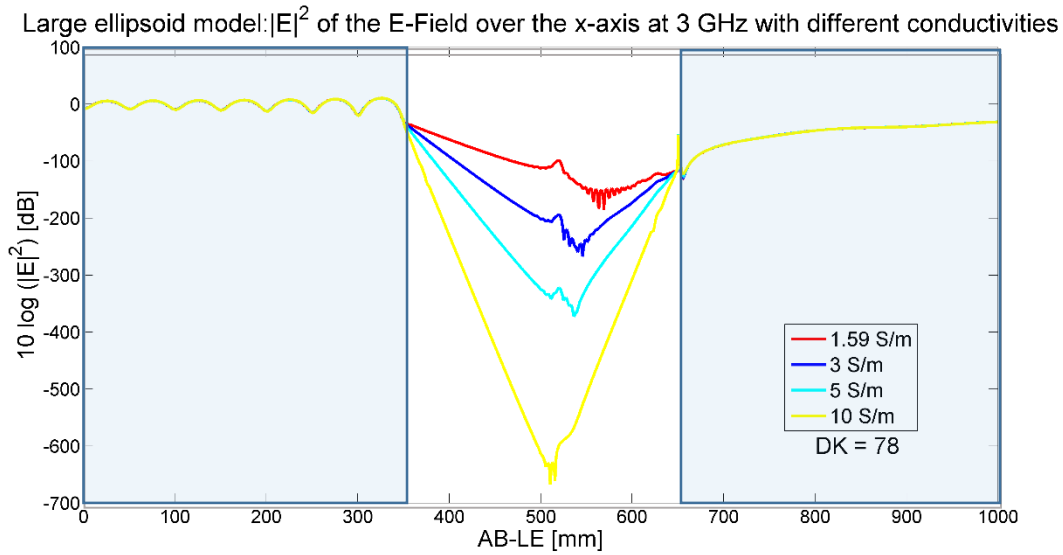


Figure 5. 20 LE model: E^2 of the E-Field over the x-axis at 3 GHz with different conductivities

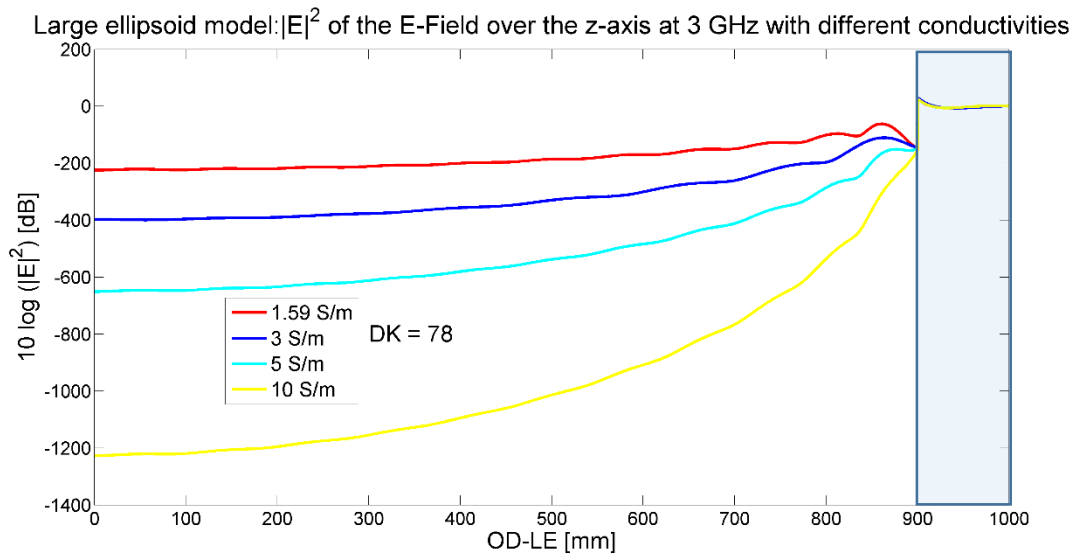


Figure 5. 21 LE model: E^2 of the E-Field over the z-axis at 3 GHz with different conductivities

Finally, the exploration of different material conductivity is discussed. This is relevant because almost all biological materials (see section 4.4) show a higher conductivity for increasing frequency [3]. Having different and increasing conductivity values will result in higher damping inside the body. This behavior is expected because the electrical conductor-like behavior is observed. Thus, less E-Field penetration, as is shown in Figures 5.20 and 5.21.

6. Conclusions and Recommendations

Full-wave simulations of simple geometrical models were evaluated in the frequency range from 1 to 10 GHz for computation of field absorption to obtain results related to point SAR and to establish a comparison between the computational requirements of each numerical technique used. From the physic perspective, all solutions are consistent with respect to electromagnetism fundamentals and expected behavior.

As expected, the computational resources needed are largely due to the size of the models in comparison to the wavelength. The geometry and size of the models are relevant due to the consideration of the overall E-field distributions inside the body because of “resonances” and attenuation that is present in media. This is notable because of the increased size of the models and how the E-field distributions changes.

The FEM based code, because of the nature of the scheme and the tool itself needs more resources with electrically large structures and the simulations could be carried out only up to 5 GHz with the simplest geometry. This is attributed to the high number of elements and resulting matrices required to obtain comparable values with respect to the other methods. Nevertheless, all methods demand an increasing amount of resources with frequency.

MoM and FIT based codes provided good and comparable results up to 10 GHz with the sphere and considering the analytical solution. Also, the results were good with the small ellipsoid models. It is notable that up to 3 GHz with the large ellipsoid model no bigger differences than 10% in the final results were observed. The MoM based code gave comparable results, in general, with less computational effort, of a least the 50 % less simulation time in comparison to FIT and at least 60% less memory consumption than FIT. The simulations turn challenging with all codes at 10 GHz due to a large amount of resources.

The results resemble the expected behavior of a bad conductor material for the analyzed objects; this behavior is more notable at higher frequencies due to the electrical properties of the water in relation to the skin effect (high damping inside the model and the reflections of the incident plane wave).

The effect of the plane wave illuminating the models can be approximated for most cases as a surface interaction because of the limited field penetration inside the body in the GHz range, attributed to the skin effect phenomena and the high damping inside the body. It is important to mention that the computation requirements increase with the frequency and the definition of the full model or in this case a quarter of the model because of the used of symmetry are not possible to consider at even higher frequencies than 10 GHz with the available resources. Therefore, for future studies, a higher amount of resources would be required, or alternative methods focused to solve this type of problems.

Because the body is much larger than the wavelength at higher frequencies, according to physic optics, it may be possible to extend a 1D multilayered model illuminated by the plane wave capable of calculating the surface impedance, and from this, use a layered method for more efficient analyses. Also, this can be complemented by using more realistic material models and geometries, with the implementation of frequency dependencies of biological materials.

References

- [1] T. Wu, T. S. Rappaport and C. M. Collins, "Safe for Generations to Come: Considerations of Safety for Millimeter Waves in Wireless Communications," in *IEEE Microwave Magazine*, vol. 16, no. 2, pp. 65-84, March 2015.
- [2] Furse, C., Christensen, D. and Durney, C. (2009). *Basic introduction to bioelectromagnetics*. 1st ed. Boca Raton, FL: CRC Press.
- [3]
G.Marin,G.Samoilescu,O.BaltagandS.Radu,"Assessmentofelectromagneticradiation exposure of embarked personnel on Romanian naval ships," *Electrical and Power Engineering (EPE), 2014 International Conference and Exposition on*, Iasi, 2014, pp.427-432.
- [4] *IEEE Standard for Safety Levels with Respect to Human Exposure to the Radio Frequency Electromagnetic Fields, 3 kHz to 300 GHz*, IEEE Standard C95.1, 2005.
- [5] ICNIRP, "Guidelines for limiting exposure to time-varying electric, magnetic, and electromagnetic fields (up to 300 GHz)," *Health Phys.*, vol. 74, no. 4, pp. 494–522, Apr. 1998.
- [6] *FCC Evaluating Compliance with FCC Guidelines for Human Exposure to Radiofrequency Electromagnetic Fields*, Federal Communications Commission Standard, OFT Bulletin 65, Edition 97-01, 1997.
- [7] ANSYS. HFSS 14.0 2017. [Online]. Available: <http://www.ansys.com>
- [8] CST. Microwave Studio 2017. [Online]. Available: <http://www.cst.com>
- [9] TET-TUHH, Technische Universität Hamburg, Electromagnetic Theory Institute. CONCEPT-II.[Online]. Available: <http://www.tet.tu-harburg.de/concept/> (April, 2017)
- [10] J. Ellison, "Water: A dielectric reference," *J. Molecular Liquids*, vol. 68, 1996.
- [11] S. Gabriel, R. W. Lau, and C. Gabriel, "The dielectric properties of biological tissues: III. Parametric models for the dielectric spectrum of tissues," *Phys. Med. Biol.*, vol. 41 , no. 11 , p. 2271 , 1996.
- [12] Hasgall PA, Di Gennaro F, Baumgartner C, Neufeld E, Gosselin MC, Payne D, Klingensböck A, Kuster N, "IT'IS Database for thermal and electromagnetic parameters of biological tissues," Version 3.0, September 01st, 2015, DOI:10.13099/VIP21000-03-0.
- [13] C. A. Balanis (2012), *Advanced Engineering Electromagnetics*, 2 Ed., Wiley, USA.

- [14] M.Clemens, T.Weiland, Discrete Electromagnetism with the Finite Integration Technique, Progress in Electromagnetics Research, PIER 32, 65-87, 2001.
- [15] R. Marklein, "The Finite Integration Technique as a General Tool to Compute Acoustic, Electromagnetic, Elastodynamic, and Coupled Wave Fields", University of Kassel, Department of Electrical Engineering/Computer Sciences, Electromagnetic Field Theory, Germany.
- [16] R.F. Harrington, Field Computation by Moment Methods, Macmillan, Co., New York, 1968
- [17] R.F. Harrington, Matrix Methods for Field Problems, Proceedings of the IEEE,vol 55,no. 2, February, 2008
- [18] Walton C. Gibson, The Method of Moments in Electromagnetics, Capman & Hall/CRC, 2005
- [19] Numerical Computation of Electromagnetic Fields,Class Material MoM,Dr-Ing H.-D Brüns, Technische Universität Hamburg-Harburg
- [20] D.Davidson, Computational electromagnetics for RF and microwave engineering, 1st ed.Cambridge: Cambridge University Press, 2005.
- [21] Mader T. (1992) "Berechnung elektromagnetischer Felderscheinungen in abschnittweise homogen Medium mit Oberflächenstromsimulation". Ph. D. Thesis, Technische Universität Hamburg (TUHH) (1992).

Appendix A: Additional Results

As a complement for the simulations result with regard to the field penetration in section 5, the following graphs show the results for middle single frequencies for the sphere and small ellipsoid models.

A.1 Sphere Model Results at 2 GHz

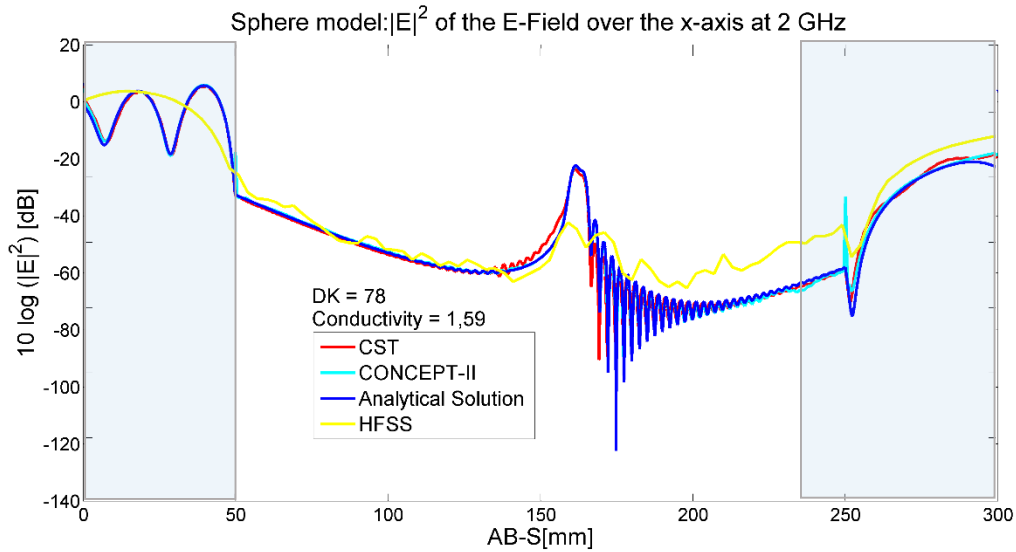


Figure A.1.1 S model: E^2 of the E-Field over the x-axis at 2 GHz

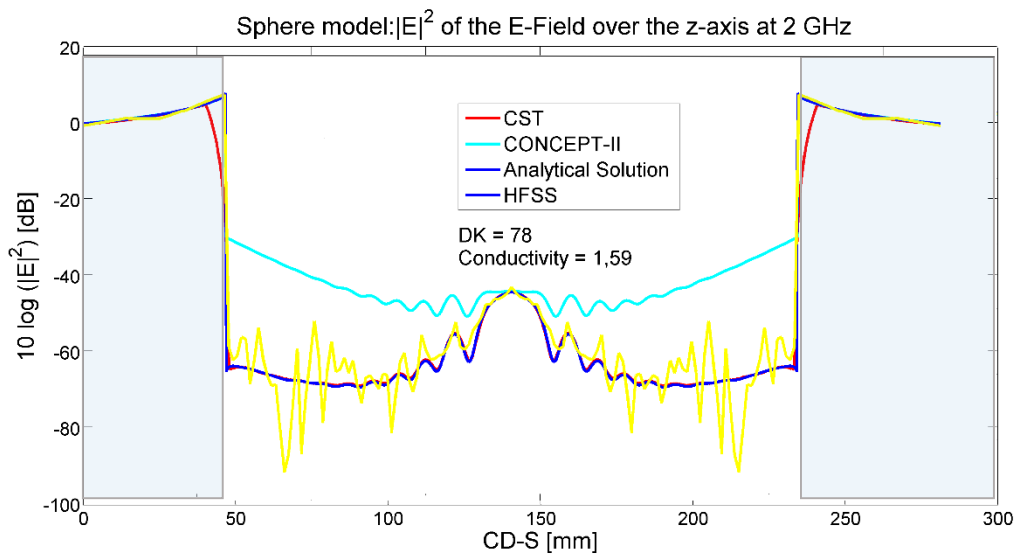


Figure A.1.2 S model: E^2 of the E-Field over the z-axis at 2 GHz

A.2 Sphere Model Results at 5 GHz

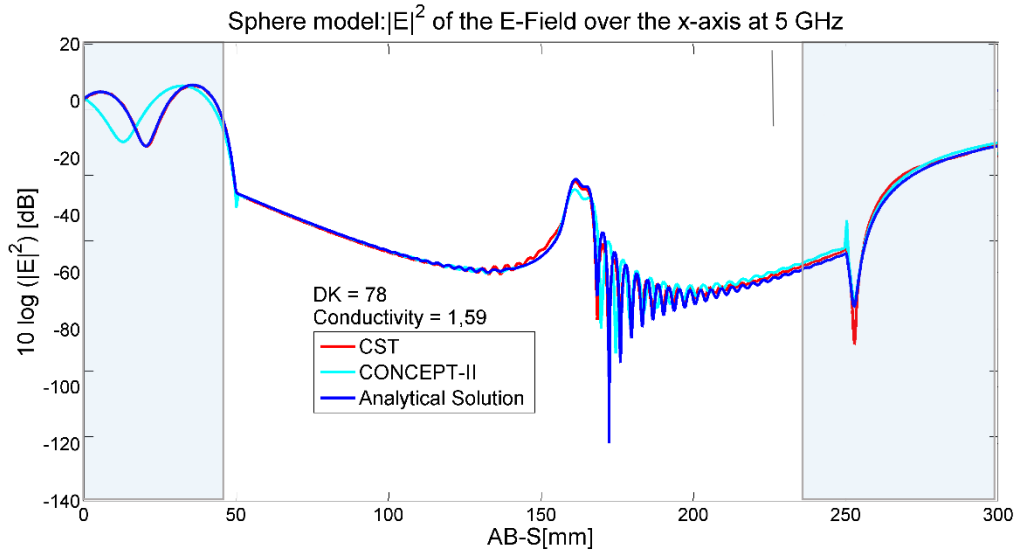


Figure A.2.1 S model: E^2 of the E-Field over the x-axis at 5 GHz

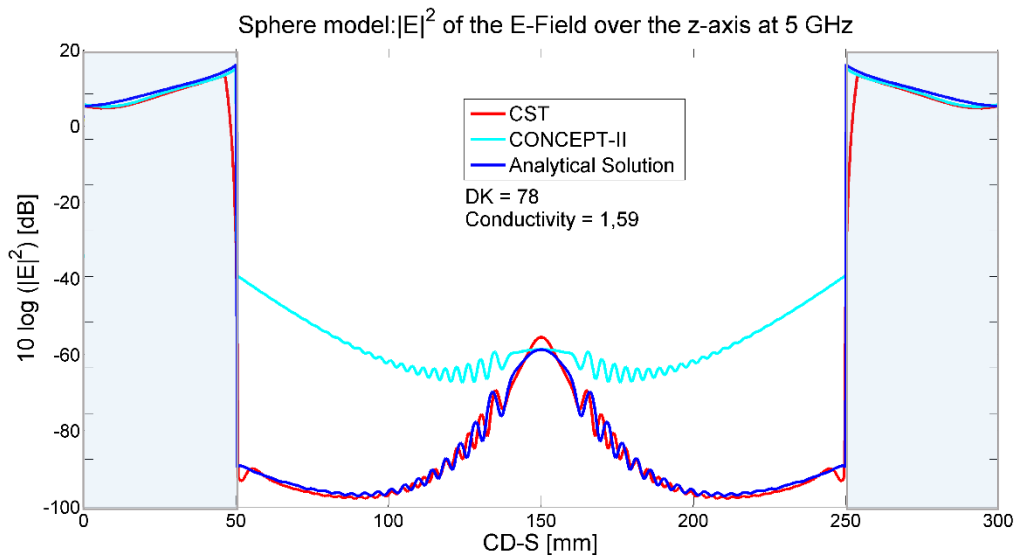


Figure A.2.2 S model: E^2 of the E-Field over the z-axis at 5 GHz

A.3 Sphere Model Results at 7 GHz

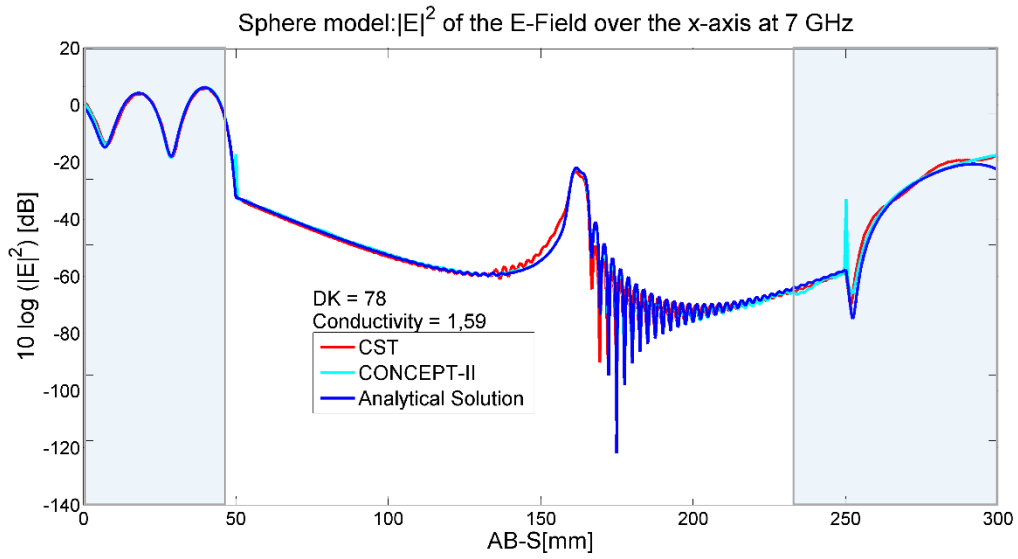


Figure A.3.1 S model: E^2 of the E-Field over the x-axis at 7 GHz

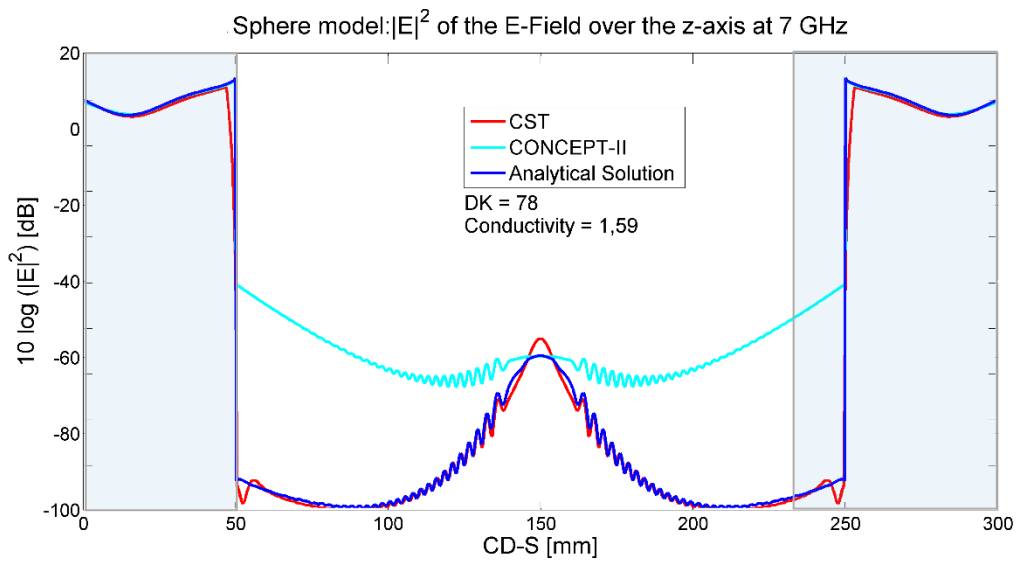


Figure A.3.2 S model: E^2 of the E-Field over the z-axis at 7 GHz

A.4 Small Ellipsoid Model Results at 2 GHz

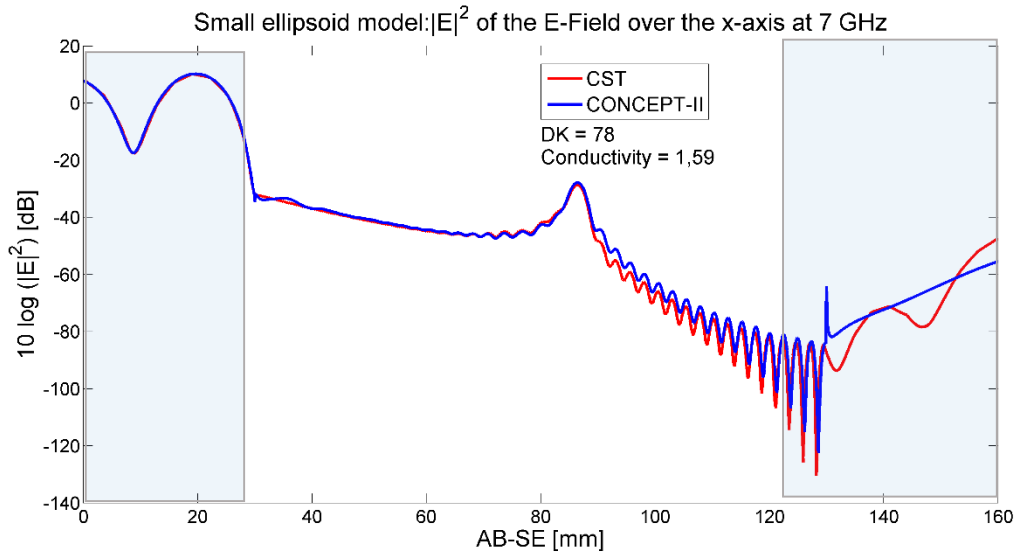


Figure A.4.1 SE model: E^2 of the E-Field over the x-axis at 2 GHz

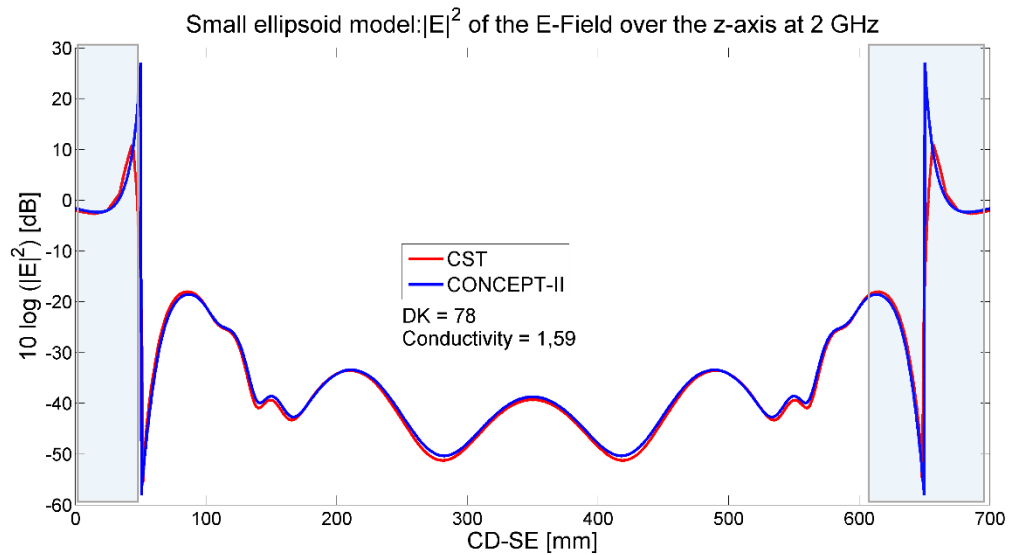


Figure A.4.2 SE model: E^2 of the E-Field over the z-axis at 2 GHz

A.5 Small Ellipsoid Model Results at 5 GHz

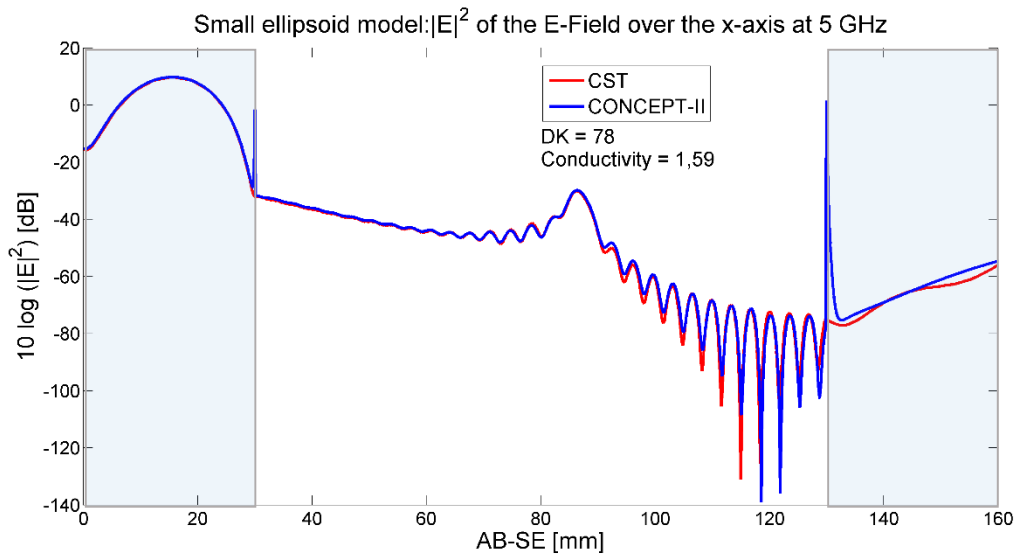


Figure A.5.1 SE model: E^2 of the E-Field over the x-axis at 5 GHz

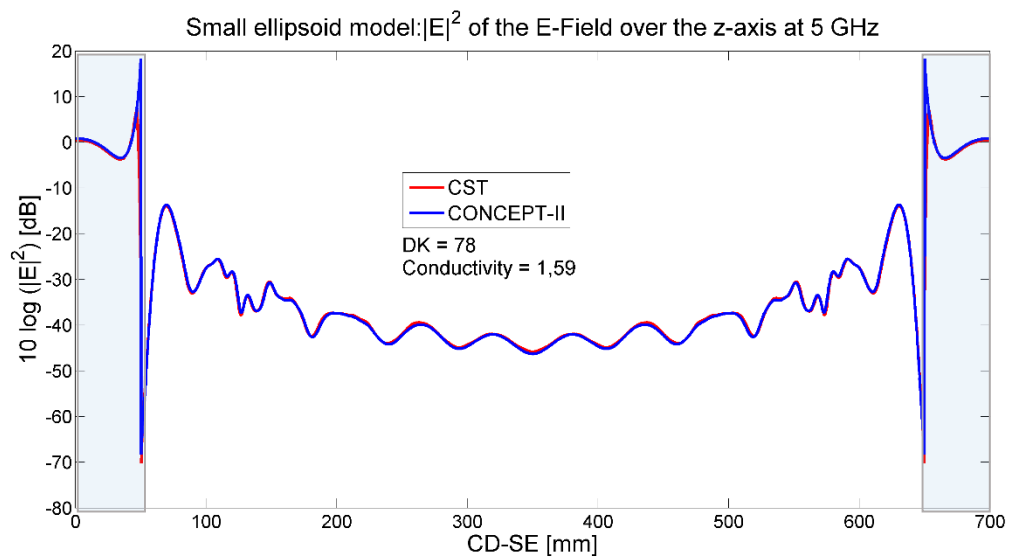


Figure A.5.2 SE model: E^2 of the E-Field over the z-axis at 5 GHz

A.6 Small ellipsoid model results at 7 GHz

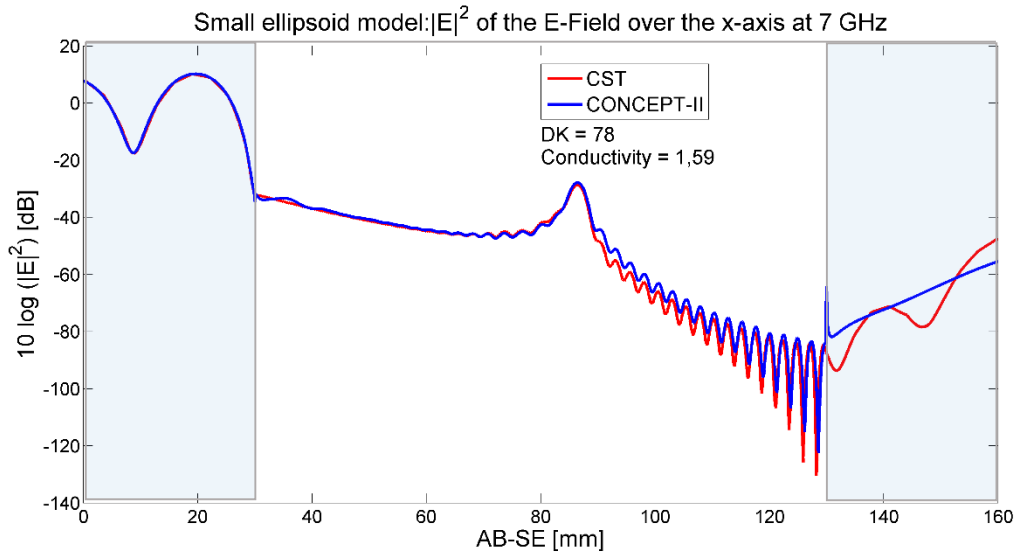


Figure A.6.1 SE model: E^2 of the E-Field over the z-axis at 7 GHz

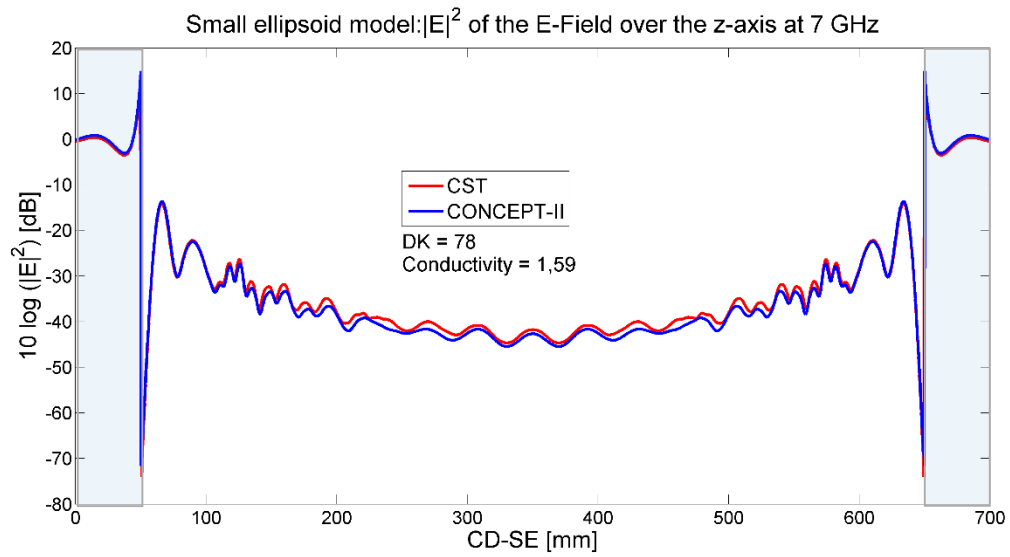


Figure A.6.2 SE model: E^2 of the E-Field over the z-axis at 7 GHz

As additional information for the simulations result about the field behavior in section 6.1, the following graphs are included. These appendix shows the results from CST and HFSS.

A.7 Sphere at 1 GHz Electric Field Distribution

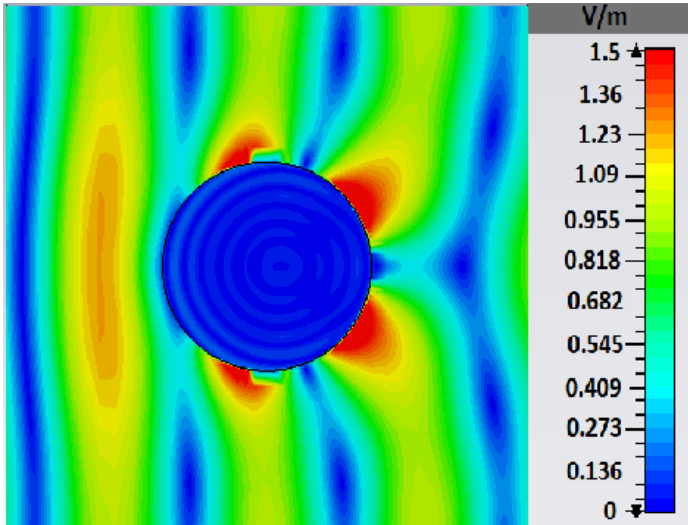


Figure A.7 XZ plane field behavior sphere model at 1 GHz in CST

A.8 Sphere at 5 GHz Electric Field Distribution

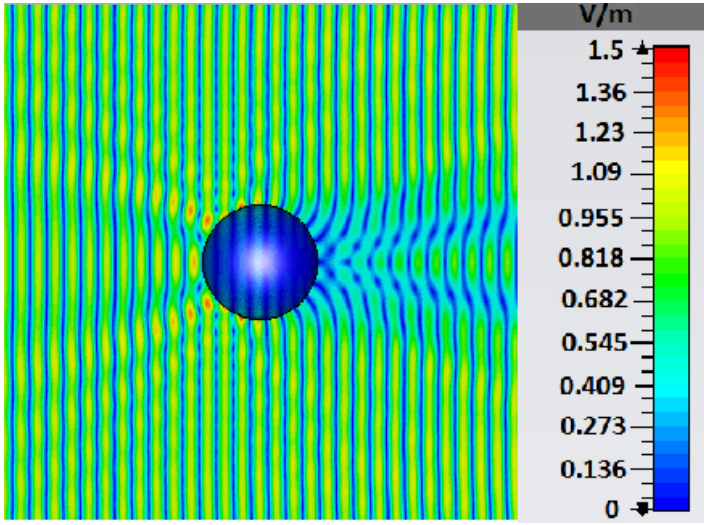


Figure A.8 XZ plane field behavior sphere model at 5 GHz in CST

A.9 Small Ellipsoid at 1 GHz Electric Field Distribution

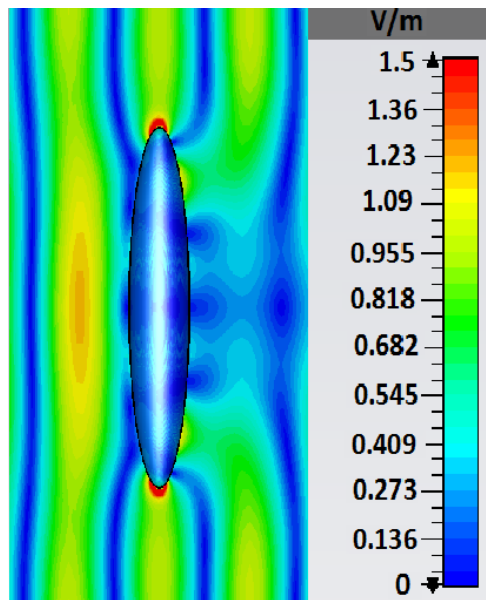


Figure A.9 XZ plane field behavior small ellipsoid model at 1 GHz in CST

A.10 Small Ellipsoid at 2 GHz Electric Field Distribution

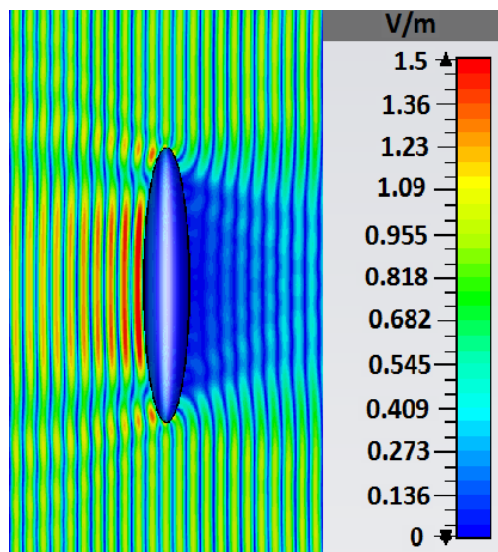


Figure A.10 XZ plane field behavior small ellipsoid model at 2 GHz in CST

A.11 Small Ellipsoid at 5 GHz Electric Field Distribution

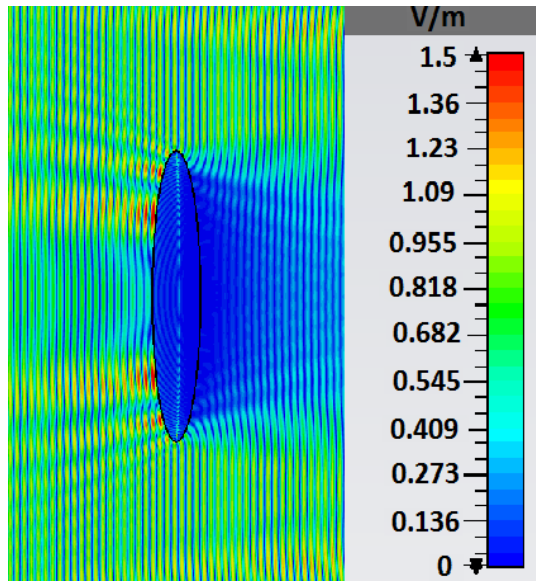


Figure A.11 XZ plane field behavior small ellipsoid model at 5 GHz in CST

A.12 Large Ellipsoid at 1 GHz Electric Field Distribution

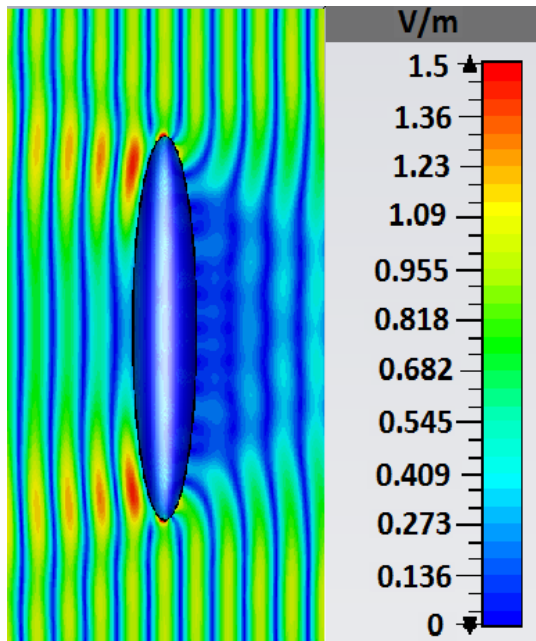


Figure A.12 XZ plane field behavior Large Ellipsoid model at 1 GHz in CST